Lithos 352–353 (2020) 105316

Contents lists available at ScienceDirect

Lithos

journal homepage: www.elsevier.com/locate/lithos

Subduction-related hybridization of the lithospheric mantle revealed by trace element and Sr-Nd-Pb isotopic data in composite xenoliths from Tallante (Betic Cordillera, Spain)

Riccardo Avanzinelli [a,b,*], Gianluca Bianchini [c,e], Massimo Tiepolo [d], Alia Jasim [a,e], Claudio Natali [a], Eleonora Braschi [b], Luigi Dallai [f], Luigi Beccaluva [c], Sandro Conticelli [a,g,*]

[a] Dipartimento di Scienze della Terra, Università degli Studi di Firenze, Via Giorgio La Pira, 4, I-50121 Firenze, Italy
[b] Istituto di Geoscienze e Georisorse, sede secondaria di Firenze, Consiglio Nazionale delle Ricerche, Via Giorgio La Pira, 4, I-50121 Firenze, Italy
[c] Dipartimento di Fisica e Scienze della Terra, Università degli Studi di Ferrara, Via Saragat 1, I-44122 Ferrara, Italy
[d] Dipartimento di Scienze della Terra, Università degli Studi di Milano "Ardito Desio", Via Botticelli 23, I-20133 Milano, Italy
[e] University of Houston Downtown, University of Houston-Downtown, One Main Street, Houston, TX 77002, USA
[f] Istituto di Geoscienze e Georisorse, sede primaria di Pisa, Consiglio Nazionale delle Ricerche, Via Giuseppe Moruzzi, 1, I-56127 Pisa, Italy
[g] Istituto di Geologia Ambientale e Geoingegneria, sede primaria di Montelibretti, Consiglio Nazionale delle Ricerche, Area della Ricerca di Roma1, Montelibretti, Via Salaria km 29,300, I-00015 Monterotondo, (RM), Italy

ARTICLE INFO

Article history:
Received 28 June 2019
Received in revised form 18 November 2019
Accepted 29 November 2019
Available online 04 December 2019

Keywords:
Betic Cordillera (Spain)
Metasomatised lithospheric mantle
Composite xenoliths
Felsic veins
Trace elements
Sr-Nd-Pb isotopes

ABSTRACT

Ultramafic xenoliths are rarely found at convergent plate margins. A notable exception is in the Betic Cordillera of southern Spain, where the eruption of xenolith-bearing alkaline basalts during the Pliocene post-dated the Cenozoic phase of plate convergence and subduction-related magmatism. Mantle xenoliths of the monogenetic volcano of Tallante display extreme compositional heterogeneities, plausibly related to multiple tectono-magmatic episodes that affected the area. This study focuses on two peculiar composite mantle xenolith samples from Tallante, where mantle peridotite is crosscut by felsic veins of different size and mineralogy, including quartz, orthopyroxene, and plagioclase. The veins are separated from the peridotite matrix by an orthopyroxene-rich reaction zone, indicating that the causative agents were alkali-rich hydrous silica-oversaturated melts, which were likely related to recycling of subducted continental crust components. The present study reports new and detailed major and trace elements and Sr-Nd-Pb analyses of the minerals in the composite Tallante xenoliths that confirm the continental crust derivation of the metasomatic melts, and clarifies the mode in which subduction-related components are transferred to the mantle wedge in orogenic areas. The particular REE patterns of the studied minerals, as well as the variation of the isotopic ratios between the different zones of the composite xenoliths, reveal a complex metasomatic process. The distribution of the different elements, and their isotope ratios, in the studied xenoliths are controlled by the mineral phases stabilised by the interaction between the percolating melts and the peridotitic country rock. The persistence of marked isotopic heterogeneities and the lack of re-equilibration suggest that metasomatism of the sub-continental lithospheric mantle occurred shortly before the xenolith exhumation. In this scenario, the studied xenoliths and the metasomatic processes that affected them may be representative of the mantle sources of mafic potassic to ultrapotassic magmas occurring in post-collisional tectonic settings.

1. Introduction

Ultramafic xenoliths provide clues on the nature of the upper mantle. In intraplate tectonic settings, the abundant occurrence of large mantle xenoliths has contributed to our understanding of the nature of both the lithospheric and asthenospheric mantle (e.g., Bonadiman et al., 2005; Downes, 2001; Pearson et al., 2003 and references therein). On the contrary, mantle xenoliths are rare and generally very small in volcanoes at destructive plate margins, hence limiting the information on mantle sources located in supra-subduction settings (e.g., Conticelli and Peccerillo, 1990; Li et al., 2018; Maury et al., 1992; Pearson et al., 2003).

A notable exception is in the Betic Cordillera of southern Spain, where decimetre-sized xenoliths were brought to the surface by the eruption of post-orogenic Na-alkaline basalts. These basalts were

* Corresponding authors at: Dipartimento di Scienze della Terra, Università degli Studi di Firenze, Via Giorgio La Pira, 4, I-50121 Firenze, Italy.
E-mail addresses: riccardo.avanzinelli@unifi.it (R. Avanzinelli), sandro.conticelli@unifi.it (S. Conticelli).

https://doi.org/10.1016/j.lithos.2019.105316

erupted during the Pliocene, after a significant phase of plate convergence, orogenesis and subduction-related magmatism (Fig. 1a) (e.g., Duggen et al., 2005; Faccenna et al., 2004; Mattei et al., 2014). The mantle xenoliths found in the volcano of Tallante, display extreme compositional and mineralogical heterogeneities, attracting an intense petrological interest that is reflected in a large number of scientific studies (e.g., Arai et al., 2003; Beccaluva et al., 2004; Shimizu et al., 2004, 2008; Martelli et al., 2011; Rampone et al., 2010; Bianchini et al., 2011, 2015; Bianchini and Natali, 2017; Marchesi et al., 2017; Dallai et al., 2019, and reference therein).

Mantle xenoliths from Tallante are mainly anhydrous and equilibrated in the spinel to plagioclase stability field (Beccaluva et al., 2004), ranging in composition from lherzolite to harzburgite. They reflect a complex history of mantle depletion and subsequent impregnation related to the migration of either alkaline (Beccaluva et al., 2004) or sub-alkaline (Bianchini et al., 2011; Rampone et al., 2010) melts.

Other samples record a peculiar style of metasomatism, rarely observed in mantle xenoliths suites world-wide, which induces orthopyroxene, plagioclase, phlogopite, and amphibole neoformation, resulting in mantle domains characterised by "hydrous" orthopyroxene-rich peridotite. The importance of these metasomatised xenoliths was recognised by Arai et al. (2003) and Beccaluva et al. (2004), who argued for subduction-related metasomatic agents.

In addition, the alkaline magmas of Tallante also exhumed rare composite xenoliths where the ultramafic matrix is locally crosscut by felsic veins containing plagioclase and orthopyroxene ± quartz ± phlogopite ± amphibole, forming phlogopite/amphibole-bearing anorthosite, diorite and gabbronorite parageneses (Arai et al., 2003; Beccaluva et al., 2004; Bianchini et al., 2011; Shimizu et al., 2004, 2005, 2008). This mineralogical association indicates that the causative melts were hydrous, silica-oversaturated and rich in alkalis, plausibly related to recycling - via subduction - of crust components within the mantle. The previous studies describing these composite xenoliths, however, did not perform a detailed isotope (Sr-Nd-Pb) study. Indeed, only few Sr—Nd isotopic data are available from a recent study by Dallai et al. (2019) which reported high $^{87}Sr/^{86}Sr$ as well as extreme $\delta^{18}O$ values (up to 10.56‰) in the felsic vein, indicating a recent recycling of crustal material within the lithospheric mantle.

Previous studies provided estimates of the conditions of last equilibration for both the anhydrous and hydrous xenoliths described above, invariably indicating a temperature and pressure range of 850 °C–1050 °C and 0.7–0.9 GPa (Bianchini et al., 2011; Rampone et al., 2010 and references therein). A minimum estimated temperature of 850 °C for the vein of the composite xenoliths was reported by Bianchini et al. (2011) on the basis of amphibole-plagioclase thermometry (Holland and Blundy, 1994).

In this paper, we have taken into consideration the best examples of composite mantle xenoliths from Tallante area (Fig. 1a), namely samples TL112 and TL189, which are characterised by centimetric size felsic veins crosscutting the ultramafic matrix. These samples show striking analogies with a sample from the same locality described by Arai et al. (2003). The selected xenoliths were characterised in extreme detail through optical observation and in-situ analytical methodologies (EMPA, LA-ICP-MS) determining i) the mineralogical distribution and

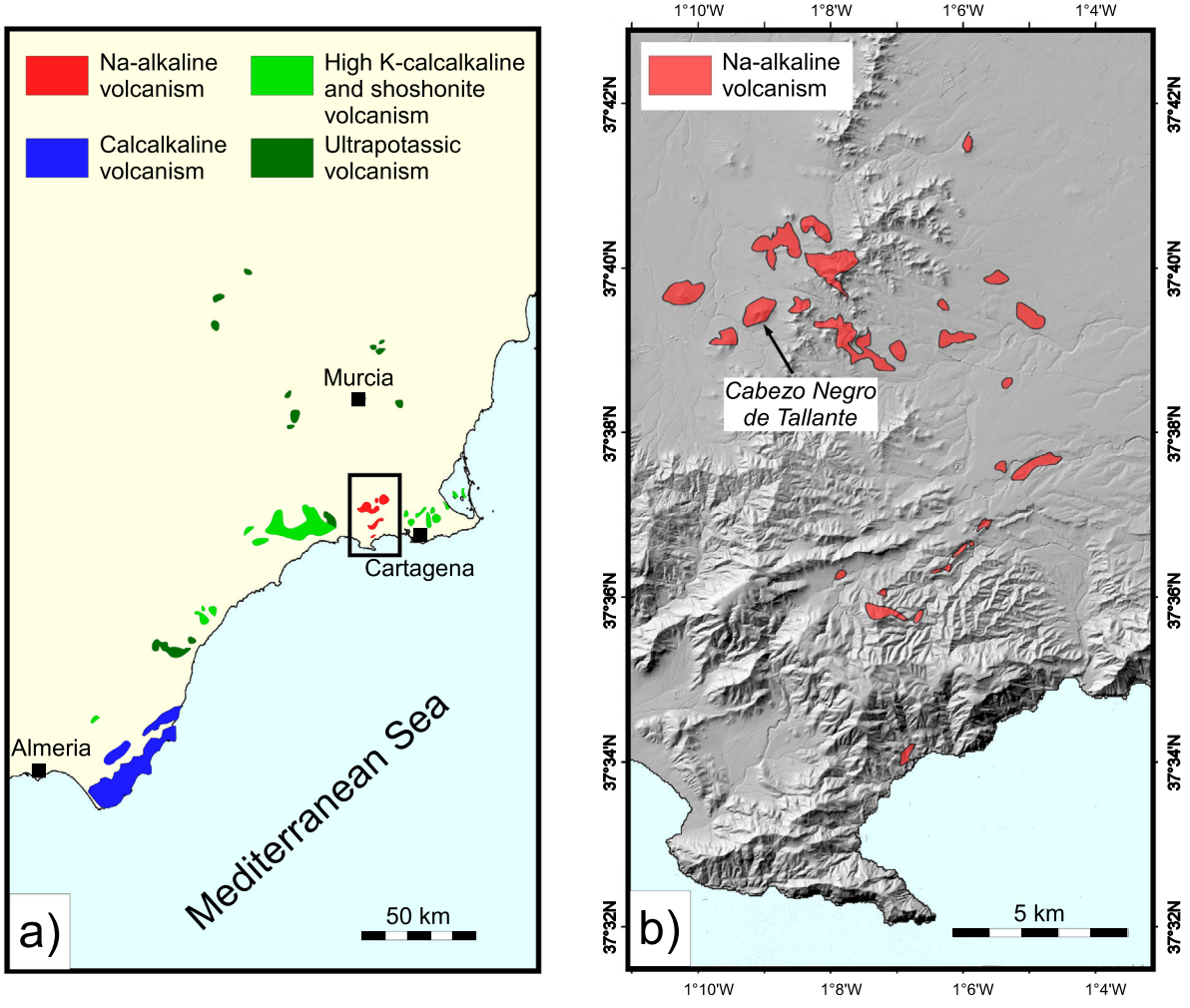

Fig. 1. a) Geographic distribution of Cenozoic magmatism in the Betic region; b) location of the Cabezo Negro de Tallante volcano hosting the studied xenoliths.

textures of the minerals in the different portions of the xenoliths (i.e. veins and surrounding peridotite) and ii) their major and trace element contents. Sr-Nd-Pb isotope analyses (TIMS) on different minerals were also determined through crystal hand picking and micro-drilling techniques. The data are used to constrain the mechanisms of mantle metasomatism by crustal-derived melts in terms of mineralogy, trace element and isotope distribution. This provides new insights on the mode in which the crustal lithologies are recycled within the mantle in collisional geodynamic settings, and on the relationship between mantle metasomatism and magma-genesis in post-orogenic convergent settings.

2. Geological outlines

The Gibraltar Arc is an arcuate orogenic region surrounding the Alboran Sea, between the Iberian and the African plates and it includes the Betic and Rif collisional belts. The Betic orogen resulted from the Tertiary closure of the westernmost sector of the Tethys Ocean and subsequent continental collision that involved the Africa and Eurasia (including Iberia) plates (Platt et al., 2013; Puga et al., 2011). The existence of a subducted slab under the area, as recorded by tomographic images and deep seismicity is still detectable (e.g., Faccenna et al., 2004; Platt et al., 2013 and references therein).

Subduction-related magmatism of Cenozoic age in the south Iberian margin has been active since the Eocene, as recorded by the Malaga dykes showing an Island Arc Tholeiite (IAT) magmatic affinity (Duggen et al., 2005; Mattei et al., 2014). After this initial magmatic phase, possibly triggered by active subduction of oceanic lithosphere, calc-alkaline and potassic volcanism resumed in orogenic and post-orogenic settings forming the South East Volcanic Province of Spain (SEVP). Calc-alkaline products erupted at Sierra de Gata (12–8 Ma), High-K calc-alkaline and shoshonitic rocks at Mazárron, and ultrapotassic rocks at Murcia (10–6 Ma)(e.g., Conticelli et al., 2009; Duggen et al., 2005; Mattei et al., 2014; Prelević et al., 2008). After a volcanic quiescence of four million years, volcanic activity resumed around the locality of Tallante in South Eastern Spain (Fig. 1a), erupting xenolith-bearing Na-alkaline basalts with a clear within-plate character (e.g., Cebriá et al., 2009).

The Cenozoic magmatism described above is closely related to the tectonic evolution of the Betic–Rif orogeny (Doblas et al., 2007 and references therein). This complex geodynamic evolution involved at least two phases: i) compression due to the continental collision of the African and Iberian plates from Upper Cretaceous to Lower Paleocene; ii) extensional episodes related to lithospheric thinning produced by isostatic readjustments and the detachment and sinking of a lithospheric root (Cebriá et al., 2009). The calc-alkaline to ultrapotassic magmatism is interpreted as emplaced under extensional conditions. The alkaline magmatism is instead suggested as deriving from a transtensional sinistral NE– SW shear zone (of NE– SW direction along the eastern margin of the Iberian Peninsula (e.g., Doblas et al., 2007 and references therein), possibly related to a change in the mantle sources from subduction related to typical within-plate related (e.g., Duggen et al., 2005).

3. Material and methods

3.1. Preliminary description of the investigated samples

The samples under consideration are both from the Cabezo Negro de Tallante (Fig. 1b), a 2 Ma old monogenetic volcano belonging to the Tallante volcanic field (e.g., Beccaluva et al., 2004; Bianchini et al., 2011). The xenoliths from Cabezo Negro de Tallante display notable and variable sizes of up to 20 cm width and variable freshness. The two composite xenoliths of this study, TL112 and TL189, were carefully recovered after slicing a sample population of 250 xenoliths. Both composite xenoliths are characterised by three well define zones, which can be observed also at the hand-specimen scale (Figs. 2a and b): i) a felsic vein; ii) a reaction zone (visible on both sides of the vein in TL189); iii) a peridotite portion. In sample TL112 a further millimetric veinlet departing from the main felsic vein can also be observed (Figs. 2a and d).

The peridotite portions of the studied composite xenoliths, at the hand-specimen scale, appear to be analogous to the unveined peridotite xenoliths observed in the same locality (e.g., Beccaluva et al., 2004). The crosscutting whitish felsic veins (and veinlet) are not to be confused with those of mafic composition, with a dark colour, mainly composed by clinopyroxene-amphibole-phlogopite assemblages, which are also recorded in other mantle xenoliths from Tallante (Bianchini et al., 2011, 2015 and references therein). These mafic veins are plausibly formed by the interaction between the peridotite and Na-alkaline mafic melts (Beccaluva et al., 2004). On the contrary, the centimetric felsic veins of samples TL112 and TL189, which are the object of this study, are likely caused by the interaction of the peridotite with silica-oversaturated melts unrelated to the host Na-alkaline basaltic magmas that carried the xenoliths to the surface.

Composite xenoliths from Cabezo Negro de Tallante with felsic veinlets were already mentioned by some authors (e.g., Beccaluva et al., 2004; Bianchini et al., 2011, 2015; Rampone et al., 2010 and references therein), but no chemical and isotopic data were provided on the vein-forming minerals. The only finding of a composite xenolith with centimetric sized veins, comparable with the TL112 and TL189 samples, was reported by Arai et al. (2003) and successively studied for trace element distribution by Shimizu et al. (2004, 2008), who suggested an adakitic nature for the felsic veins. Noteworthy, the xenoliths from Cabezo Negro de Tallante also include samples totally composed by a gabbroic lithology (mainly norite) suggesting that veins analogous to those of samples TL112 and TL189 can reach decimetric size.

3.2. Analytical techniques

Major element of minerals were determined by Electron-microprobe analyses in two laboratories using different EMPA instruments, namely i) the Dipartimento di Scienze della Terra of the Università degli Studi di Milano, with a JEOL 8200 Super Probe, and ii) the EMPA laboratory of the CNR - Istituto di Geoscienze e Georisorse at Padova, with a Camebax. The analytical conditions used were 15 kV accelerating voltage, 10 nA beam current focused beam of about 2 μm (for plagioclase the beam was defocused at 5 μm); counting times were 10 s for Na, in order to avoid alkali loss during the analytical routine, 15 s for other major elements, and 40 s for minor elements. Bias between different laboratories was evaluated using international reference samples and was evaluated to be better than 5%. More than fifty microprobe WDS analyses were integrated with nearly sixty EDS analyses, performed by Secondary Electron Microscopy (SEM) at the Dipartimento di Scienze della Terra of Università degli Studi di Firenze and at the Dipartimento di Scienze della Terra dell'Ambiente e delle Risorse of the Università degli Studi di Napoli, Federico II. In Table 1 we report the median value of the distinct mineral phases in different textural domains of each sample, whereas the complete dataset is reported as Electronic Supplementary Materials-1.

Trace elements contents of the minerals were determined through Laser Ablation (LA) ICP-MS at the at the laboratory of the CNR - Istituto di Geoscienze e Georisorse U.O.S. Pavia using a laser ablation system working at 266 nm (see Tiepolo et al., 2003 for details) connected to a quadrupole ICP-MS system DRCe from Perkin Elmer. NIST-SRM612 was used as an external standard, whereas ^{43}Ca or ^{29}Si were adopted as internal standards, depending on the analysed mineral. Repeated measures of standards (BCR-2) give an error <10%. The high sensitivity of the instrument and the limited contribution of the matrix ensured low detection limit of a few ppb for heavy elements and between 10 and 100 ppb for light elements (Tiepolo et al., 2003). Representative

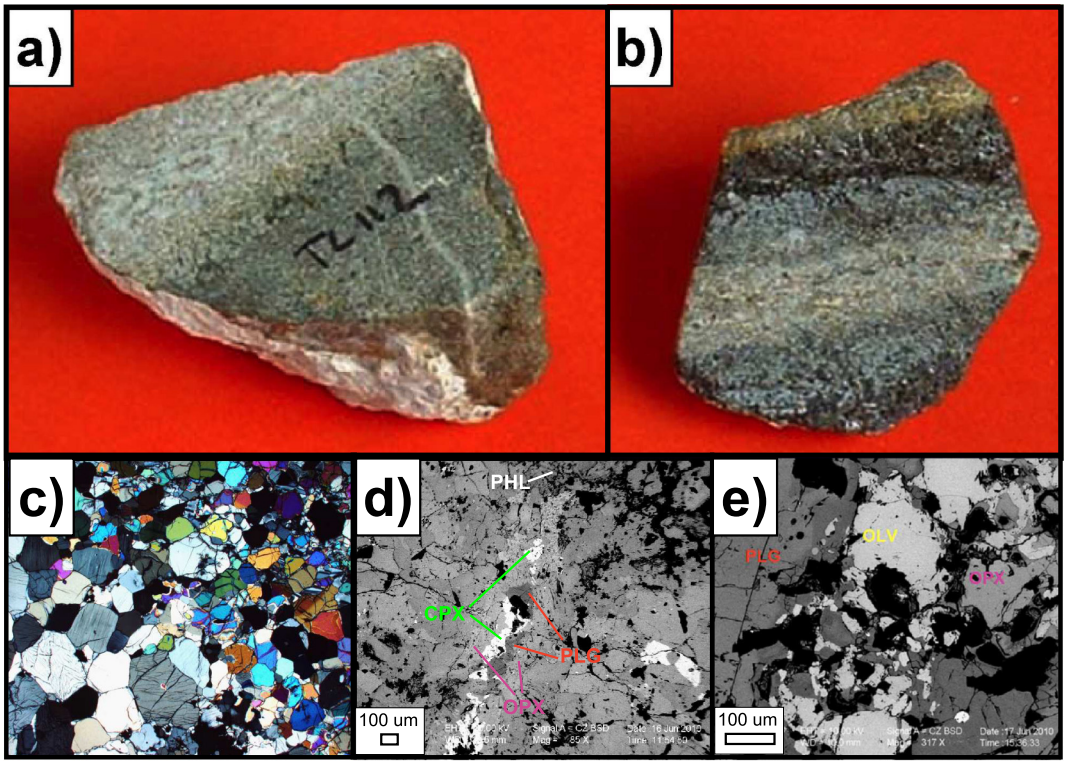

Fig. 2. a) Composite xenolith TL112, including peridotite portion (bottom right), reaction zone and centimetric vein (top left); the millimetric felsic veinlet is also visible: b) Composite xenolith TL189 where the centimetric felsic vein is sandwiched on both sides by an inner reaction zone and an outer peridotite portion; c) OM (crossed polarised light) image showing the transition between peridotite (top right) and reaction zone (bottom left) in TL112; d) SEM image (back-scattered electron) of the millimetric felsic veinlet in TL112; e) SEM image (back-scattered electron) of the centimetric vein of TL189.

trace element analyses are reported in Table 2, whereas the complete set of data is reported as Electronic Supplementary Materials-2.

Sr, Nd and Pb ratios (Table 3) were determined at the Dipartimento di Scienze della Terra of the Università degli Studi di Firenze. Most of the measured samples were obtained by mineral separations of distinct phases by hand picking, in order to avoid the effect of different mineral abundances in different portions of the samples. One measurement on the micrometric veinlet of sample TL112 was performed by drilling the sample in situ (Di Salvo et al., 2018) with a MicroMill™ device (Merchantek-New Wave Research). Measurements were done on micro-quantities of powder using a specific loading and measure procedure (Di Salvo et al., 2018). Mineral separates were digested and then the solutions purified through standard liquid chromatographic techniques. Sr, Nd, and Pb isotopic ratios were measured by thermal ionization mass spectrometry (TIMS) using a Thermo-Finnigan Triton TI© as described in Avanzinelli et al. (2005). Mass fractionation of Sr and Nd isotopes has been exponentially corrected with $^{86}Sr/^{88}Sr = 0.1194$ and $^{146}Nd/^{144}Nd = 0.7219$, respectively. The within-run $^{87}Sr/^{86}Sr_{triple}$ average value for NBS 987 reference sample was 0.710247 ± 9 (2σ, $n = 6$), and the $^{143}Nd/^{144}Nd_{triple}$ average value for the internal standard NdFi was 0.511471 ± 9 (2σ, n = 6). Mass bias for Pb isotope measurements was monitored with repeated

Table 1
Median major element composition of the mineral phases in the studied composite xenolith samples.

	TL 112											TL 189									
Lithology	Peridotite				Reaction zone		Felsic vein		Felsic veinlet			Peridotite				Reaction zone			Felsic vein		
Mineral	Ol	Opx	Cpx	Pl	Opx	Pl	Opx	Pl	Opx	Cpx	Pl	Opx	Cpx	Pl	Sp	Opx	Pl	Sp	Ol	Opx	Pl
n	2	3	1	1	2	3	3	8	3	1	2	3	4	2	2	5	2	1	3	3	6
SiO_2 *(wt%)*	41.0	56.1	51.5	51.7	55.4	56.4	57.8	62.8	55.8	54.4	58.2	53.2	49.3	42.5	0.0	53.5	53.6	0.3	39.2	52.9	53.6
TiO_2	bdl	0.3	0.5	0.0	0.5	0.1	0.1	bdl	0.2	0.0	0.0	0.3	1.2	bdl	0.2	0.3	bdl	0.1	0.0	0.3	0.0
Al_2O_3	0.0	3.6	5.1	30.2	4.6	27.2	0.6	23.4	2.5	0.6	26.6	4.3	5.3	35.0	58.2	5.8	27.7	63.3	0.0	5.3	29.3
Cr_2O_3	bdl	0.6	1.0	bdl	0.5	0.0	0.1	bdl	0.3	bdl	0.0	0.3	0.5	0.1	10.4	0.2	bdl	1.6	0.0	0.1	0.0
FeO	10.1	6.5	2.3	0.2	7.3	bdl	9.6	0.1	6.7	3.1	0.1	7.9	2.9	0.3	12.3	10.3	0.5	15.0	19.3	11.8	0.1
MnO	0.1	0.2	0.0	bdl	0.1	bdl	0.2	bdl	0.2	0.2	0.0	0.1	0.1	0.0	0.1	0.2	bdl	0.1	0.3	0.2	0.0
NiO	0.4	0.1	bdl	bdl	0.1	0.0	0.1	bdl	0.1	0.1	bdl	0.1	0.1	0.0	0.4	0.1	bdl	0.4	0.2	0.1	0.0
MgO	48.4	32.5	15.7	0.2	32.5	0.1	32.0	0.0	32.0	17.2	0.1	30.0	15.0	0.4	19.2	29.3	0.5	18.0	41.1	28.2	0.1
CaO	bdl	0.9	21.8	13.1	0.5	10.7	0.9	5.1	0.9	23.3	8.4	0.6	22.0	18.0	0.0	0.4	9.9	bdl	0.1	0.5	12.0
Na_2O	0.0	bdl	0.6	3.5	bdl	5.6	0.0	7.7	0.0	0.2	6.2	0.1	0.3	0.6	bdl	0.1	4.9	0.0	0.0	0.0	4.7
K_2O	bdl	nd	bdl	0.1	bdl	0.1	bdl	1.1	0.0	bdl	0.4	0.0	0.0	0.2	bdl	0.0	0.1	bdl	0.0	bdl	0.1
Total	100.1	101.0	98.6	99.0	101.4	99.6	101.5	100.7	99.5	99.3	100.0	96.9	96.7	97.3	100.9	100.8	97.3	98.8	100.6	99.4	99.4

The table reports the median values of the WDS (EMPA) measurements made, for each mineral phase, in the differenrt zones of the studied samples. Ol: olivine; Opx: orthopyroxene; Cpx: clinopyroxene: Pl: plagioclase: Sp: spinel; n: number of analyses; bdl = below detection limit. The full dataset is reported as Electronic Supplementary Materials (ESR-1).

Table 2
Median trace element composition of the mineral phases in the studied composite xenolith samples.

	TL 112											TL 189							
Lithology	Peridotite				Reaction zone		Felsic vein		Felsic veinlet			Peridotite			Reaction zone		Felsic vein		
Mineral	Ol	Opx	Cpx	Pl	Opx	Pl	Opx	Pl	Opx	Cpx	Pl	Opx	Cpx	Pl	Opx	Pl	Opx	Pl	Cpx
n	7	4	6	6	7	2	9	12	3	2	2	8	6	2	47	10	9	15	1
Li *(ppm)*	5.65	5.39	10.6	17.8	9.09	8.20	8.94	14.7	3.62	3.16	2.41	5.61	5.13	bdl	4.95	2.05	3.94	2.12	3.45
Be	1.12	bdl	3.10	9.96	0.55	bdl	bdl	0.86	1.39	bdl	5.71	0.65	0.54	bdl	0.47	1.04	0.37	0.71	bdl
B	2.32	1.56	2.27	3.56	1.29	1.05	1.03	3.15	2.20	1.72	3.93	1.60	2.83	bdl	2.05	2.06	1.20	1.11	1.17
Sc	3.24	20.8	49.3	1.82	21.9	1.56	18.66	2.70	15.2	13.2	1.74	19.8	48.1	0.62	23.8	1.9	25.5	1.08	142
Ti	25.7	1270	2893	98.0	1049	207	707	162	361	172	70.6	1691	6134	62.0	1539	166	1038	52.7	1087
V	1.84	131	239	1.93	116	1.69	109	1.88	42.5	30.0	6.23	101	196	1.59	121	3.84	224	1.02	1079
Cr	35.1	4368	6745	88.0	3368	28.0	693	4.77	378	28.3	bdl	1887	3102	3.63	1602	12.2	374	3.52	2549
Co	143	53.8	25.1	0.31	63.6	0.56	83.2	0.31	72.6	33.6	1.19	59.6	21.5	0.44	71.9	1.89	70.2	0.36	25.1
Ni	2807	548	325	9.97	588	20.0	1109	49.4	1005	1471	217	695	331	66.3	607	115	566	22.8	342
Zn	57.9	44.0	16.5	3.26	50	2.21	74.1	2.03	61.6	17.3	2.83	57.0	12.7	1.02	83.8	3.75	70.8	1.10	25.9
Rb	0.04	bdl	0.06	1.44	0.04	2.38	0.06	6.69	0.19	0.55	17.3	0.05	0.05	0.12	0.04	1.06	0.51	0.69	0.06
Sr	0.15	0.23	20.2	183	0.05	56.4	0.10	72.5	0.58	7.70	188	0.10	2.38	41.2	0.03	203	1.98	209	7.02
Y	0.08	8.31	84.7	0.27	16.2	0.92	18.1	1.03	6.07	54.9	0.60	10.8	137	0.57	12.1	0.98	8.80	0.37	49.9
Zr	0.06	7.02	49.4	0.47	7.26	0.57	1.77	0.73	0.74	10.8	0.43	15.2	164	bdl	13.6	0.67	11.6	0.19	41.1
Nb	0.03	0.03	0.81	0.1	0.04	0.26	0.03	0.6	0.08	0.29	0.15	0.06	1.45	bdl	0.02	0.11	0.02	0.03	0.03
Cs	bdl	bdl	0.03	0.04	0.01	0.08	0.00	0.11	0.03	0.03	0.39	0.01	0.01	0.03	bdl	0.02	0.01	0.02	bdl
Ba	0.09	0.08	bdl	23.7	0.04	27.7	0.12	75.8	0.58	0.77	30.0	0.06	0.04	39.8	0.04	59.6	0.94	64.5	bdl
La	0.01	0.01	1.65	1.56	0.01	0.94	0.01	2.39	0.21	10.2	16.5	0.02	1.62	0.76	0.01	3.46	0.03	4.75	1.57
Ce	0.09	0.04	8.77	3.27	0.03	2.64	0.05	5.09	0.13	29.5	24.1	0.04	10.1	2.34	0.02	5.70	0.07	7.19	7.45
Pr	0.01	0.03	1.87	0.24	0.03	0.35	0.01	0.45	0.05	3.85	1.46	0.02	3.32	0.24	0.01	0.45	0.02	0.59	1.49
Nd	0.04	0.09	13.3	0.54	0.07	1.20	0.06	1.73	0.26	18.0	4.09	0.14	37.6	1.49	0.09	1.52	0.08	1.90	10.1
Sm	0.05	0.31	11.5	0.14	0.35	0.81	0.22	0.67	0.12	7.31	0.5	0.40	34.2	0.45	0.27	0.43	0.14	0.49	7.48
Eu	bdl	0.03	0.67	1.04	0.01	1.05	0.01	1.30	0.03	0.38	1.23	0.02	1.46	1.6	0.02	1.93	0.04	1.78	1.79
Gd	0.10	0.63	22.9	0.20	1.62	0.70	1.13	0.75	0.29	12.9	0.33	0.83	44.1	0.27	0.98	0.41	0.52	0.27	9.21
Tb	0.02	0.17	3.84	0.01	0.46	0.09	0.34	0.09	0.11	2.36	0.05	0.22	6.70	0.02	0.26	0.05	0.15	0.02	1.53
Dy	0.04	1.24	21.1	0.03	2.83	0.37	2.83	0.39	0.92	12.8	0.20	1.55	34.4	0.08	2.02	0.22	1.31	0.10	9.16
Ho	bdl	0.32	3.45	0.03	0.70	0.03	0.69	0.04	0.26	2.31	0.02	0.41	5.66	bdl	0.45	0.03	0.38	0.01	2.05
Er	0.03	1.01	7.52	bdl	1.80	bdl	2.04	0.06	0.56	4.77	0.04	1.23	12.0	0.05	1.37	0.07	1.09	0.03	5.48
Tm	0.01	0.15	0.80	0.01	0.26	0.01	0.29	0.01	0.13	0.53	bdl	0.21	1.33	bdl	0.23	0.01	0.21	bdl	0.80
Yb	0.09	0.98	4.66	0.13	2.03	0.08	2.28	0.06	1.16	3.16	bdl	1.42	6.79	bdl	1.65	0.05	1.41	0.03	6.67
Lu	0.02	0.17	0.53	0.05	0.26	bdl	0.35	0.01	0.18	0.32	0.01	0.23	0.78	bdl	0.26	0.01	0.24	0.01	0.90
Hf	bdl	0.23	1.27	bdl	0.21	bdl	0.11	0.06	0.05	0.45	bdl	0.42	3.56	bdl	0.34	0.07	0.28	0.02	1.31
Ta	0.01	0.00	0.05	0.02	0.01	0.01	0.00	0.08	0.01	0.05	0.01	bdl	0.19	bdl	bdl	0.01	0.01	0.01	bdl
Pb	0.05	0.03	0.06	1.47	0.03	0.62	0.03	4.18	0.10	0.67	11.3	0.04	0.05	0.94	0.02	4.62	0.09	3.27	0.20
Th	0.01	0.02	0.72	0.04	0.02	0.05	0.01	0.32	0.07	1.00	0.40	0.02	1.58	bdl	0.02	0.05	0.05	0.02	2.01
U	bdl	0.01	0.30	0.02	0.01	bdl	0.02	0.20	0.03	0.22	0.06	0.02	0.60	0.02	0.02	0.03	0.04	0.01	0.69

The table reports the median values of the LA-ICPMS measurements made, for each mineral phase, in the differenrt zones of the studied samples. Ol: olivine; Opx: orthopyroxene; Cpx: clinopyroxene: Pl: plagioclase: Sp: spinel; n: number of analyses; bdl = below detection limit. The full dataset is reported as Electronic Supplementary Materials (ESR-2) along with replicate analyses of certified standard materials.

measurements of the SRM 981 reference standard and we obtained a mass discrimination factor (ε) of 0.15% per a.m.u. Accuracy and reproducibility were monitored through replicate measurements of international standard AGV-1, with values of $^{208}Pb/^{204}Pb = 38.566 \pm 56$, $^{207}Pb/^{204}Pb = 15.654 \pm 15$ and $^{206}Pb/^{204}Pb = 18.941 \pm 13$; ($2\sigma$, $n = 14$). All data are provided as Electronic Supplementary Materials–3. All data are provided as Electronic Supplementary Materials–3..

4. Results

4.1. Petrography and mineral chemistry

The peridotite portions of the studied composite xenoliths TL112 and TL189 display protogranular textures with an average crystal size around one millimetre, resembling the textures of the unveined peridotite xenoliths found in the same locality and extensively described in the literature (e.g., Beccaluva et al., 2004; Bianchini et al., 2011; Marchesi et al., 2017; Rampone et al., 2010, and references therein). In the studied samples the felsic veins are invariably mantled by orthopyroxene, as already described by some authors (Arai et al., 2003; Beccaluva et al., 2004; Rampone et al., 2010; Shimizu et al., 2004, 2008).

Under the microscope four different domains were recognised in the studied samples: 1) the peridotite portion, 2) the orthopyroxene-rich transition, hereafter "*reaction zone*", 3) the main felsic vein, and 4) the millimetric veinlet departing from the main felsic vein and found only in sample TL112 (Fig. 2a and d).

4.1.1. Petrography and mineral chemistry of peridotite domain of composite xenoliths

The peridotite portion of the sample TL112 has a harzburgitic composition (Fig. 3), containing prevalent olivine (~75 vol%), subordinate orthopyroxene (~ 20 vol%), and minor clinopyroxene (< 5 vol%); spinel is absent and Ca-rich plagioclase was found only as an interstitial phase. The peridotite portion of the sample TL189 has a lherzolitic composition (Fig. 3), containing prevalent olivine (~ 70 vol%), subordinate orthopyroxene (~ 18 vol%) and clinopyroxene (~ 9 vol%) with accessory amount of spinel (~ 3 vol%). The peridotitic portions of both samples fall close to the boundary between lithospheric spinel lherzolite and harzburgite together with the other ultramafic xenoliths exhumed at Tallante (Fig. 3; e.g., Beccaluva et al., 2004; Bianchini et al., 2011; Dallai et al., 2019).

Olivine is highly forsteritic ranging from $Fo_{89.8}$ to $Fo_{88.2}$ in the TL112 harzburgite and $Fo_{86.0}$ in the TL189 lherzolite (Fig. 4a). These Fo values are slightly lower than those recorded in the unveined anhydrous peridotite xenoliths from the Tallante site (i.e., $Fo_{91.6}$-$Fo_{88.9}$; Beccaluva et al., 2004).

Orthopyroxene within the peridotite portion of both composite xenoliths is characterised by Mg-rich compositions with $En_{87.4–88.3}$ $Fs_{10.0–10.7}$

Table 3
Sr, Nd and Pb isotope composition of the studied composite xenolith samples.

TL 112															
Label	Lithology	Material	$^{87}Sr/^{86}Sr$	2 s.e.	$^{143}Nd/^{144}Nd$	2 s.e.	$^{206}Pb/^{204}Pb$	2 s.e.	$^{207}Pb/^{204}Pb$	2 s.e.	$^{207}Pb/^{204}Pb$	2 s.e.	Δ7/4	Δ8/4
Tl 112–4	Peridotite	Cpx separate	0.706051	0.000007	0.512597	0.000005	–	–	–	–	–	–	–	–
TL112 –2	Reaction Zone	Opx separate	0.707703	0.000010	–	–	–	–	–	–	–	–	–	–
TL112–5	Centrimetric Vein	Plg separate	0.712429	0.000004	0.512527	0.000005	18.844	0.013	15.668	0.015	39.981	0.058	13.4	157.2
TL112–5 repl			*0.712439*	*0.000006*	–	–	–	–	–	–	–	–	–	–
TL 112–6	Millimetric veinlet	Bulk	0.707519	0.000006	0.512567	0.000005	–	–	–	–	–	–	–	–
TL112–5 repl			*0.707509*	*0.000010*	–	–	–	–	–	–	–	–	–	–
MD3–TL 112	Millimetric veinlet	Microdrilled Bulk	0.708124	0.000012	–	–	–	–	–	–	–	–	–	–
Previously published data (Dallai et al., 2019)							–	–	–	–	–	–	–	–
TL112	*Peridotite*	*Cpx separate*	*0.70588*	*0.00001*	*0.51260*	*0.00001*	–	–	–	–	–	–	–	–
TL112	*Centimetric Vein*	*Plg separate*	*0.71266*	*0.00001*	*0.51260*	*0.00002*	–	–	–	–	–	–	–	–

TL 189														
Label	Lithology	Material	$^{87}Sr/^{86}Sr$	2 s.e.	$^{143}Nd/^{144}Nd$	2 s.e.	$^{206}Pb/^{204}Pb$	2 s.e.	$^{207}Pb/^{204}Pb$	2 s.e.	$^{207}Pb/^{204}Pb$	2 s.e.	Δ7/4	Δ8/4
Tl 189–12	Peridotite	Cpx separate	0.707843	0.000006	0.512271	0.000004	–	–	–	–	–	–	–	–
Tl 189–11	Peridotite	Opx separate	0.707705	0.000009	–	–	–	–	–	–	–	–	–	–
TL189–10	Reaction Zone	Plg separate	0.708219	0.000006	–	–	18.820	0.013	15.681	0.015	39.016	0.057	15.0	63.6
TL189–8	Reaction Zone	Opx separate	0.707695	0.000010	–	–	–	–	–	–	–	–	–	–
TL189–8 repl			*0.707698*	*0.000014*	–	–	–	–	–	–	–	–	–	–
TL189–7	Centrimetric vein	Opx separate	0.707597	0.000006	–	–	–	–	–	–	–	–	–	–
TL189–9	Centrimetric vein	Plg separate	0.707631	0.000005	0.512457	0.000004	18.890	0.013	15.715	0.015	39.158	0.057	17.6	69.3
TL189–9 repl			0.707632	0.000006	–	–	–	–	–	–	–	–	–	–
TL 189–15	Centrimetric vein	Bulk	0.707822	0.000007	0.512502	0.000011	–	–	–	–	–	–	–	–

Sr and Nd isotopes were measured at the Radiogenic Isotopes Laboratory of the University of Firenze (Avanzinelli et al., 2005) with a Thermo Finnigan Triton Thermal Ionisation Mass Spectrometer (TIMS) in multi-dynamic mode. Internal errors on sample data (± 2 s.e) are fully propagated for all the corrections applied. Pb isotope ratios were measured with the same instrument of Sr and Nd. Mass bias was corrected by replicate analyses of NIST SRM 981 as described in Avanzinelli et al., 2005. The internal errors (± 2 s.e) on the samples' ratio are calculated from the reproducibility of AGV 1 standards (see Electronic Supplementary Material -3). Delta values represent the difference the 207Pb/204Pb and 208Pb/204Pb and the Northern Hemisphere Reference Line (NHRL: Hart, 1984).

$Wo_{1.0–2.6}$ in the TL112 harzburgite and $En_{84.8–86.1}$ $Fs_{12.4–13.7}$ $Wo_{1.0–1.8}$ in the TL189 lherzolite (Fig. 4b).

Clinopyroxene has a diopsidic composition with the few crystals from the TL112 harzburgite having a higher enstatite component ($En_{47.9–49.9}$ $Fs_{4.1–4.9}$ $Wo_{45.6–48.0}$ in TL112) than those from the TL189 lherzolite ($En_{44.7–46.5}$ $Fs_{4.7–5.9}$ $Wo_{48.2–49.9}$). These values are comparable with those recorded in the unveined anhydrous peridotite xenoliths from Tallante (Beccaluva et al., 2004).

Plagioclase, found only interstitially in the peridotite of the TL112 composite xenolith, has a labradorite composition (Fig. 4c) with an anorthite content ($An_{66.9}$) higher than that found in the unveined anhydrous peridotite xenoliths from Tallante ($An_{58.4–61.5}$).

Spinel was found only in the peridotite portion of the TL189 lherzolite, with a Cr# between 0.08 and 0.11, a value significantly lower than that found in the unveined anhydrous peridotite xenoliths from Tallante (Cr# 0.17–0.24; Beccaluva et al., 2004).

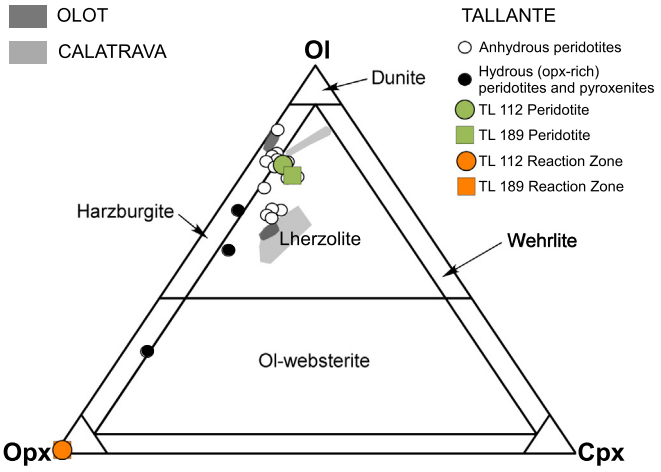

Fig. 3. Modal composition of the peridotite portions and the reaction zones of the studied composite xenoliths. Also reported are the compositions of both anhydrous and hydrous (opx-rich) mantle xenoliths from Tallante (data from Beccaluva et al., 2004). Fields represent the composition of xenoliths from other Spanish volcanic occurrences (data from Bianchini et al., 2007, 2010).

4.1.2. Petrography and mineral chemistry of felsic veins and surrounding reaction zones

4.1.2.1. Sample TL112. This composite xenolith is characterised by the occurrence of two felsic veins of different width. The larger felsic vein, centimetric in width, shows a granoblastic texture with a mineral paragenesis dominated by plagioclase (~60 vol%) and orthopyroxene (~35 vol%) with minor amounts of quartz and clinopyroxene (~5 vol%). Graphite was also recorded as an accessory phase by Bianchini and Natali (2017).

The smaller felsic veinlet, millimetric in width, is clearly related to the larger one, but shows a more complex mineralogy (Fig. 2d). It is dominated by large quartz crystals, elongated along the direction of the veinlet, which makes up about 40 vol% of the visible veinlet. The quarts crystals are surrounded by orthopyroxene (~10 vol%), clinopyroxene (~7 vol%) and olivine (~3 vol%), as well as phlogopite (~3 vol%), the latter found as euhedral hexagonal dark lamellae. The remaining portion of the veinlet is made up by symplectite patches

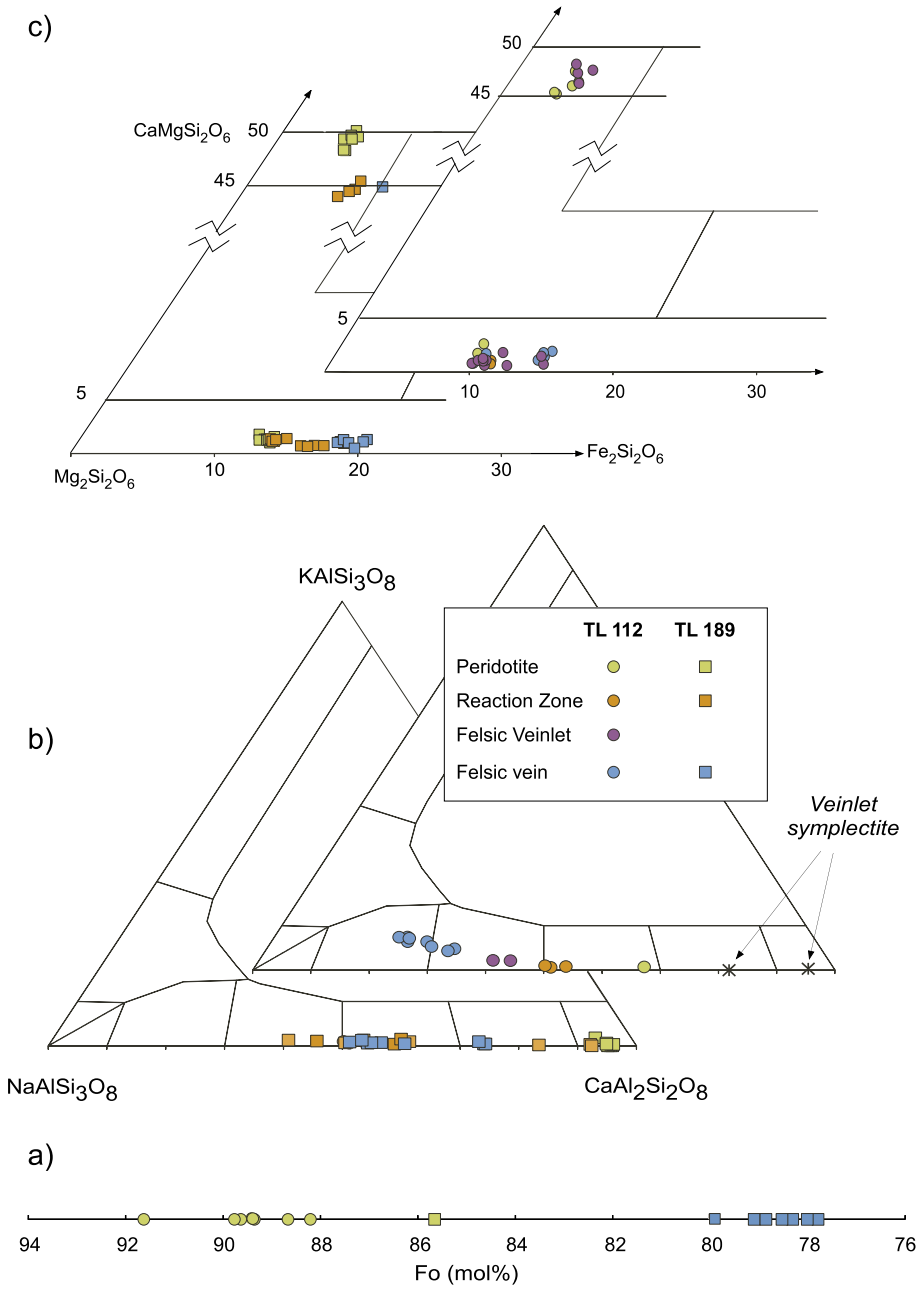

Fig. 4. Mineral chemistry of the studied composite xenoliths: a) forsterite content of olivine; b) triangular classification diagram of plagioclase; c) clinopyroxene classification on the base of quadrilateral components (Morimoto, 1989).

composed of a micrometre/submicrometre-scale intergrowth of orthopyroxene and plagioclase. These types of symplectite have never been observed in mantle xenolith suites from other locations, and more generally are not a common petrological feature. Indeed, orthopyroxene-plagioclase symplectite were observed only in anatectic frameworks, as results of dehydration melting of garnet bearing crustal lithologies (e.g., Neogi et al., 1998).

The orthopyroxene of the main felsic vein in TL112 is characterised by a composition slightly, but distinctly, enriched in Fe ($En_{83.0–84.5}$ $Fs_{14.6–15.1}$ $Wo_{1.1–1.9}$) with respect to the orthopyroxene of the peridotite portion (Fig. 4b). The orthopyroxene within millimetric felsic veinlet is enriched in the enstatite component ($En_{84.0–89.3}$ $Fs_{10.1–13.0}$ $Wo_{0.6–1.8}$), suggesting partial equilibration with the host peridotite matrix. The most Mg-rich compositions are found in the orthopyroxene from the symplectite (Electronic Supplementary Materials-1).

The plagioclase of the main felsic vein is characterised by homogeneous andesine composition ($An_{22.9–32.3}$), whereas in the millimetric felsic veinlet there is a clear distinction between large equilibrated crystals (andesine, $An_{40.2–43.2}$) and microcrystals from the symplectite aggregates that are strongly enriched in Ca with a composition straddling the bytownite-anorthite fields ($An_{81.8–95.3}$)(Fig. 4b).

The clinopyroxene found within the millimetric veinlet has a composition comparable to that of the crystals found in the peridotitic portion of the same sample ($En_{45.7–48.1}$ $Fs_{3.8–5.3}$ $Wo_{46.8–48.1}$), but with significantly lower Al_2O_3 (Fig. 4c).

An important characteristic of the millimetric veinlet is the presence of accessory minerals such as apatite, thorite/huttonite, rutile, and graphite, which suggests a late-stage crystallisation of this felsic domain, approaching the “closure” of the metasomatic melt percolation. Noteworthy, thorite/huttonite are generally observed as accessory

phases in pegmatites associated with granitoids, and/or in high-grade metamorphic rocks and migmatites (e.g., Pérez-Soba et al., 2014).

The reaction zone between peridotite and the main felsic vein is made up by few millimetres of orthopyroxene with equigranular, polygonal texture and triple junctions between the euhedral crystals. The reaction zone shows a transition from the peridotite towards the vein (Fig. 2c), where the equigranular orthopyroxene is gradually permeated by plagioclase. As the amount of infilling plagioclase increases, the orthopyroxene crystal size decreases and the crystals shapes become less defined with curved contacts.

4.1.2.2. Sample TL189. This composite xenolith is characterised by the occurrence of a single centimetric felsic vein, showing a granoblastic texture (Fig. 2e) with dominant plagioclase (~70 vol%), subordinate orthopyroxene (~20 vol%) and olivine (< 10 vol%), and accessory clinopyroxene.

The plagioclase composition varies from labradorite to bytownite ($An_{50.9–73.9}$) with sodium enrichment from the rim of the vein towards its core (Fig. 4c). Olivine ($Fo_{77.8–79.9}$) crystals are engulfed by plagioclase forming poikilitic texture, and are characterised by a consistently higher fayalite component with respect to the olivine from the peridotitic portion. The amount of orthopyroxene crystals ($En_{78.4–80.6}$ $Fs_{18.6–20.3}$ $Wo_{0.5–1.3}$) decreases in parallel with a slight compositional change from the rim of the vein (Mg# = 83–84) towards its core (Mg# = 80–82), whereas the rare clinopyroxene has an $En_{45.4}$ $Fs_{9.9}$ $Wo_{44.7}$ composition.

The paragenesis of the felsic vein of the TL189 composite xenolith is characterised by the occurrence of accessory amphibole and spinel, the latter with a peculiar Fe—Ti enrichment (FeO up to 34.5 wt%, TiO_2 up to 7.8 wt%) and Al depletion (Al_2O_3 down to 11.5 wt%) with respect to that recorded in the surrounding peridotitic portion. The felsic vein is armoured by an orthopyroxenite reactions zone, which is also clearly visible in the hand specimen (Fig. 2b).

On the whole, it seems that the metasomatic melts rose up along dykes that cut the overlying mantle. Metasomatic melts were characterised by silica-oversaturation, which promoted the reaction of olivine to orthopyroxene. The process also induced destabilisation of diopside and spinel that were gradually replaced by plagioclase. Subsequently, in the inner part of the vein, the metasomatic process continued inducing plagioclase-orthopyroxene co-crystallisation. Finally, amphibole crystallised as an accessory phase.

In summary, these veins plausibly contain both newly formed phases crystallised from the metasomatic melt and relics of pre-existing minerals forming the peridotite country rock that were partially re-equilibrated with the metasomatic agents.

4.2. Trace elements

More than one hundred LA-ICP-MS trace element analyses were carried out on the different textural domains of the composite xenoliths TL112 and TL189, i.e. in the peridotites, in the main felsic veins (decametric width) and in the reaction zones, as well as in the late millimetric felsic ones of sample TL 112. The median values of distinct minerals in the different textural domains are reported for each sample in Table 2 whereas the complete dataset is reported in Supplementary Materials-2.

4.2.1. Trace element composition of minerals in the peridotite

In this section the main features, in terms of trace element contents, of the mineral phases analysed in the peridotite portion of the studied composite xenoliths are described in comparison with those of the more common unveined (anhydrous) mantle xenoliths from Tallante (e.g., Beccaluva et al., 2004; Rampone et al., 2010), which were plausibly not affected by the vein-related metasomatic processes.

4.2.1.1. Clinopyroxene. Clinopyroxene in peridotite rocks is usually the main carrier of incompatible trace elements and is commonly analysed to extrapolate the petrogenetic evolution of mantle domains. Among trace elements, emphasis is generally given to Rare Earth Elements (REE) that have a well-constrained geochemical behaviour. REE distribution in clinopyroxene in peridotite depends on temperature, pressure, and mineral composition (e.g., Witt-Eickschen and O'Neill, 2005). Generally, REE patterns of clinopyroxene from "primitive" spinel-peridotite mantle domains are characterised by a concentration of ~10–15 times larger than (x) chondrite for all REE (e.g., Bianchini et al., 2014; Bonadiman et al., 2005; Downes, 2001; Pearson et al., 2003; Scott et al., 2016). Depletion in the Light (L) REE, which are more incompatible with respect to Heavy (H) REE (i.e. $La_N/Yb_N < 1$), is generally ascribed to partial melting and melt extraction, whilst enrichment in LREE with respect to HREE (i.e. $La_N/Yb_N > 1$) is often related to metasomatic processes (e.g., Bianchini et al., 2007; Downes, 2001). The REE composition of clinopyroxene from the peridotite portion of the composite xenoliths from Tallante is not readily explicable in the context of single-stage metasomatism or melt extraction. As shown in Fig. 5a and b, peculiar M-shaped REE patterns are recorded in the clinopyroxene of the peridotite portion of TL112 and TL189. They have very high H-REE (up to 35 x chondrite) and ultra-high Middle (M)-REE (up to 200 x chondrite). They show strong LREE/MREE and MREE/HREE fractionation with extreme values of La_N/Sm_N (0.07–0.26 and 0.029–0.032 in TL112 and TL189, respectively) and Gd_N/Yb_N (2.8–5.7 and 4.7–5.6, respectively), and a remarkable negative anomaly in Eu ($Eu/Eu^* = 0.09–0.31$ and 0.10–0.14, respectively). These REE patterns are significantly different to those reported for clinopyroxene hosted in the unveined anhydrous peridotite xenoliths of Tallante (e.g., Beccaluva et al., 2004; Rampone et al., 2010), which show relatively flat patterns generally at <10 x chondrite values (Fig. 5a and b). Similar M-shaped patterns, although less extreme, were noted among the suite of Tallante xenoliths in some orthopyroxene-rich, amphibole bearing xenoliths (Beccaluva et al., 2004) and in another composite xenolith studied by Shimizu et al. (2004, 2005); as far as we know, similar patterns have never been recorded in clinopyroxene from other peridotite mantle rocks worldwide.

Sr is strongly depleted, similarly to Eu, especially when compared with clinopyroxene of the unveined anhydrous peridotite mantle xenoliths of the same area (i.e., Cabezo Negro de Tallante; Figs. 5a and b), suggesting an important role for coexisting plagioclase. Y (53–99 ppm and 118–142 ppm in clinopyroxene from TL112 and TL189, respectively) is also very high with respect to what observed in anhydrous xenoliths (< 32 ppm, Beccaluva et al., 2004; Rampone et al., 2010).

Compatible trace elements such as Sc (46–59 ppm and 47–50 ppm in TL112 and TL189, respectively) and V (216–253 ppm and 192–198 ppm in TL112 and TL189, respectively) are similar in both samples, and they fall well within the range of clinopyroxene of the Tallante unveined anhydrous peridotite xenoliths (Rampone et al., 2010). Chromium is significantly higher in the clinopyroxene of the TL112 sample (6499–7290 ppm) than in that of the TL189 sample (2787–3138 ppm), which is consistent with the occurrence, in the latter, of Cr-rich spinel.

4.2.1.2. Orthopyroxene. Orthopyroxene in peridotite mantle domains usually has sub-chondritic REE concentration (e.g., Bonadiman et al., 2011; Ionov et al., 2013; Scott et al., 2016).

As delineated for clinopyroxene, the REE contents of orthopyroxene in peridotite rocks can be used to highlight partial melting and melt extraction that generally induce LREE depletion, or metasomatic processes that induce LREE enrichment (Bianchini et al., 2014; Scott et al., 2016).

The distribution of REE in orthopyroxene from the peridotite portion of the studied composite xenoliths (Fig. 5c and d), although being depleted in LREE ($La_N/Sm_N = 0.06–0.08$ and 0.02–0.4 in TL112 and TL 189, respectively), show several other features that distinguish it from that of "typical" mantle xenoliths. In particular, the HREE are almost flat with Gd_N/Yb_N in the range 0.4–0.7 and 0.4–0.8 for TL112 and TL189, respectively. These ratios are significantly higher than those

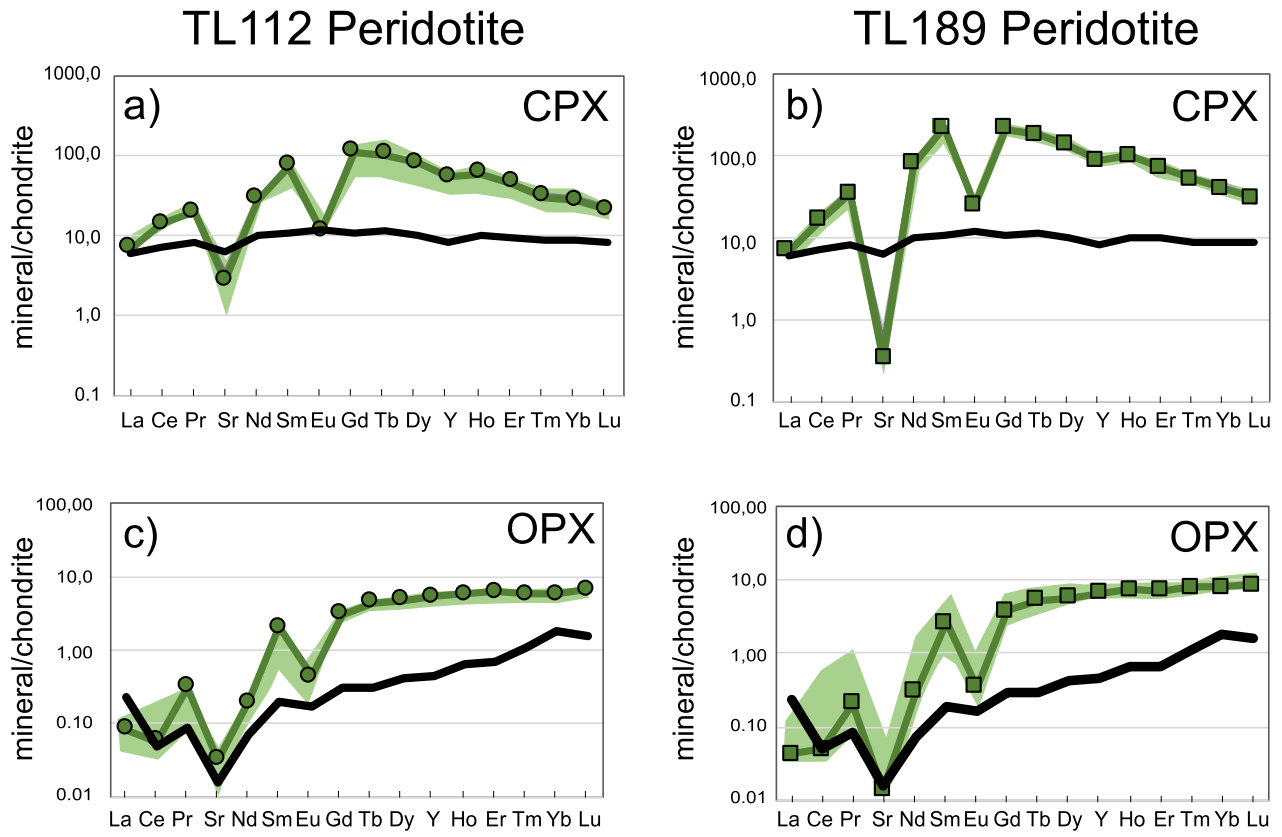

Fig. 5. Chondrite-normalised Rare Earth Element (REE) patters, plus Sr and Y, of orthopyroxene (OPX) and clinopyroxene (CPX) in the peridotite portion of the studied composite xenoliths, compared with that of anhydrous xenoliths from Tallante (black lines, median of the data from Beccaluva et al., 2004). Solid green lines with symbols represent the median values of pyroxenes data for TL112 (a and c) and TL189 (b and d); the shaded green areas cover the whole data variability. Normalising values after Sun (1989). (For interpretation of the references to colour in this figure legend, the reader is referred to the web version of this article.)

reported for the anhydrous mantle xenolith of Tallante where $Gd_N/Yb_N < 0.15$ (Fig. 5c and d), and also different to theoretical melting models that predict lower starting compositions and marked fractionation of the patterns during melt extraction (Scott et al., 2016). The observed features in orthopyroxene are thus impossible to explain with common processes like melt extraction, similar to what is observed in the coexisting clinopyroxene.

The occurrence of the Eu negative anomaly in orthopyroxene (Eu*/Eu <0.2 in both TL112 and TL189), as well as its low Sr content (<0.5 ppm) is consistent with what is observed in clinopyroxene, suggesting again the main role of plagioclase in sequestering these elements. As observed for clinopyroxene, the Y contents of orthopyroxene (6.9–9.4 ppm and 10.4–14.5 ppm in TL112 and TL189, respectively) is consistently higher than that reported for the same mineral in unveined anhydrous xenoliths (< 1.6 ppm, Beccaluva et al., 2004).

4.2.1.3. Olivine. Olivine trace element contents were measured only on sample TL112 (Table 2, Supplementary Materials-2). Since no trace element data on olivine crystals is reported for the unveined anhydrous xenoliths from Tallante, we used the detailed study of Rampone et al. (2016) on olivine from oceanic peridotites for comparison. The olivine from the peridotite portion of the studied Tallante composite xenoliths has Ni (2726–3085 ppm in TL112) and Co (141–147 ppm in TL112) contents comparable to those of the oceanic peridotite reported by Rampone et al. (2016). On the contrary, the studied Tallante olivines are extremely enriched in Li (3.7–6.6), up to 6 times more elevated than those of oceanic peridotites (Rampone et al., 2016), representing the highest concentration ever recorded in mantle olivine (Rampone et al., 2016 and references therein). This argues for a felsic nature of the metasomatic agents that are enriched in Li with respect to mafic melts (Neukampf et al., 2019). Indeed, comparably high Li was also found in magmatic olivine from K-rich mafic rocks erupted at destructive plate margins, where the mantle experienced crustal metasomatism (e.g., Ammannati et al., 2016; Foley et al., 2011). REE distribution of olivine crystals of the peridotite portion of TL112 is also characterised by higher REE (especially LREE) concentration with respect to that of peridotite mantle rocks impregnated by MORB-type melts (Rampone et al., 2016).

4.2.1.4. Plagioclase. REE distribution of plagioclase crystals in the peridotite portion of composite xenolith TL112 (no plagioclase was found in the peridotite portion of TL189) is consistently characterised by Sr and Eu positive anomaly (Eu/Eu* up to 34) as well as high La_N/Sm_N (up to 11.2). This LREE enrichment is not observed in peridotite mantle rocks impregnated by MORB-type melts (Rampone et al., 2016). Overall the patterns of plagioclase are antithetic to those of pyroxenes (Fig. 6) indicating that the metasomatic process responsible for the vein formation affected also the peridotite portion surrounding them.

4.2.2. Trace element composition of minerals in felsic veins and surrounding reaction zones

4.2.2.1. Clinopyroxene. Clinopyroxene was found and analysed only in the millimetric veinlet of TL112, and it shows H– to MREE distribution (Gd_N/Yb_N = 3.1–3.6, Eu/Eu* = 0.11–0.13) similar to those of the clinopyroxene found in the peridotite portion, at slightly lower concentration (Fig. 6). On the other hand, clinopyroxene from the millimetric veinlet does not show the LREE depletion (La_N/Sm_N = 0.8–1.2) observed in the peridotite portion. Other trace elements, such as Y (47–54 ppm), Sc (10–12 ppm), V (18–39 ppm), and Cr (36–127 ppm)

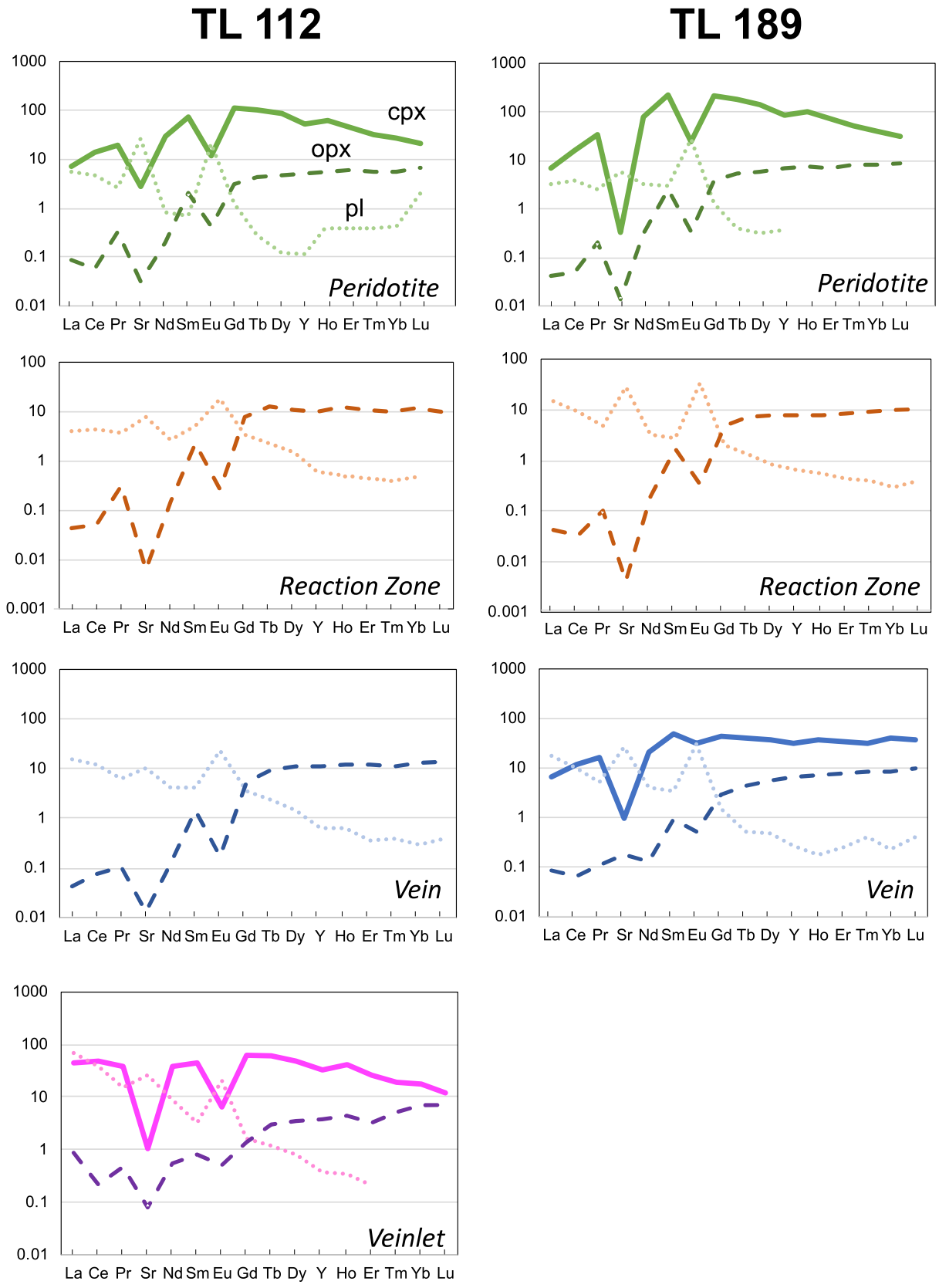

Fig. 6. Chondrite-normalised Rare Earth Element Patters, plus Sr and Y, of plagioclase (pl), orthopyroxene (opx) and clinopyroxene (cpx) in the different zones of the studied composite xenoliths. Each line represents the median values as reported in Table 2. Normalising values after Sun (1989).

are significantly lower than those measured in the peridotite portion of the same sample.

4.2.2.2. Orthopyroxene. Orthopyroxene in the reaction zone and in the centimetric felsic veins has REE and trace element patterns similar to that found in the peridotite portion of the same composite xenoliths, showing depleted LREE and flat M- to HREE patterns. In the veinlet of TL112, orthopyroxene has higher LREE contents, similar to what is observed for clinopyroxene (Fig. 6). Other trace element contents are also generally similar to those recorded in the peridotite domain and do not show significant variations between the reaction zone, the centimetric veins and the veinlet. The only exceptions are represented by i) Cr, which in both samples is lower in the reaction zone and even further in the vein, ii) V, which in sample TL189 shows the opposite behaviour slightly increasing towards the vein, and iii) Sr that is also higher in the vein (especially in TL189).

4.2.2.3. Plagioclase. Plagioclase in the main felsic veins, centimetric in width, and in the reaction zones of TL189 have similar trace element patterns (Fig. 6), with positive LREE/MREE (La_N/Sm_N up to 12), Eu/Eu* (up to 21), and positive Sr anomaly (e.g., Sr_N/Nd_N up to 25) (Fig. 7). In sample TL112, the plagioclase of the main felsic vein has La_N/Sm_N similar to that measured in the plagioclase of its peridotite portion, and slightly higher than that of plagioclase found in the reaction zone. Eu/Eu* and Sr_N/Nd_N are significantly lower in the main felsic vein and reaction zone than in the surrounding peridotite portion. The larger enrichment in compatible elements in the plagioclase of the surrounding peridotite portion, with respect to that of the main felsic veins, is likely due to the different proportions of this mineral with respect to the other. Indeed, in the main felsic vein, and to a lesser extent in the reaction zone, the large amounts of crystallising plagioclase compete to incorporate the available amount of Sr and Eu. On the contrary, in the peridotite, the much more limited amount of interstitial plagioclase crystals are able to sequester these element with little competition. Conversely, incompatible element such as LREE, but also Ba and Rb are generally more enriched in the vein with respect to the peridotite and the reaction zone (Table 2, Supplementary Materials-2). In comparison to TL189, plagioclase of the vein (and reaction zone) of TL112 has generally lower La_N/Sm_N, Eu/Eu* and Sr_N/Nd_N.

Plagioclase crystallised in the millimetric veinlet of composite xenolith TL112 has patterns similar to those of the plagioclase of the main felsic vein, although at higher LREE contents and thus higher La_N/Sm_N (up to 33). This is consistent with what is observed for pyroxenes, suggesting that the millimetric veinlets were related to the interaction with final (residual) melt fractions enriched in LREE and incompatible trace elements, as demonstrated also by the presence in these veinlet of accessory phases such as monazite thorite/huttonite, zircon and rutile.

4.3. Radiogenic isotopes

$^{87}Sr/^{86}Sr$ and $^{143}Nd/^{144}Nd$ of the peridotite portion of both composite xenoliths were measured on clinopyroxene separates giving values of 0.706051 ± 6 and 0.512597 ± 6, respectively, in TL112, and of 0.707843 ± 6 and 0.51271 ± 4, respectively, in TL189 (Table 3). In TL189 we also measured $^{87}Sr/^{86}Sr$ in orthopyroxene mineral separate from the peridotite portion (0.707705 ± 9) surrounding the felsic vein that matches the value measured in clinopyroxene.

Sr isotope compositions in the reaction zones were measured on both plagioclase and orthopyroxene separates of sample TL189 with the former showing a slightly higher value (0.708219 ± 6 and 0.707695 ± 10, respectively), and only in the orthopyroxene separate in sample TL112 (0.707703 ± 10).

For the vein of TL189 we measured Sr and Nd isotope ratios in a plagioclase separate (0.707631 ± 7, 0.512457 ± 4) and a bulk portion of the whole vein (0.707822 ± 7, 0.512502 ± 4). A further Sr measurement on orthopyroxene yielded isotope ratios very similar to that of the plagioclase (0.707697 ± 6).

The centimetric felsic veins of TL112 yielded a high $^{87}Sr/^{86}Sr$ (0.712249 ± 4) and low $^{143}Nd/^{144}Nd$ (0.512527 ± 4) measured on separated plagioclase crystals. The millimetric veinlet of the same sample was measured for Sr and Nd isotopes by handpicking it after crushing (0.707519 ± 6, 0.512567 ± 5). A further Sr isotope measurement (0.708124 ± 12) was performed by directly drilling in situ along the centre of the millimetric veinlet with a modern MicroMill™ drilling device.

Pb isotopes were performed only on plagioclase separates from the main felsic veins of both samples and also from the reaction zone of TL189. The results are similar to each other and plot at high $^{207}Pb/^{204}Pb$, well above the Northern Hemisphere Reference Line

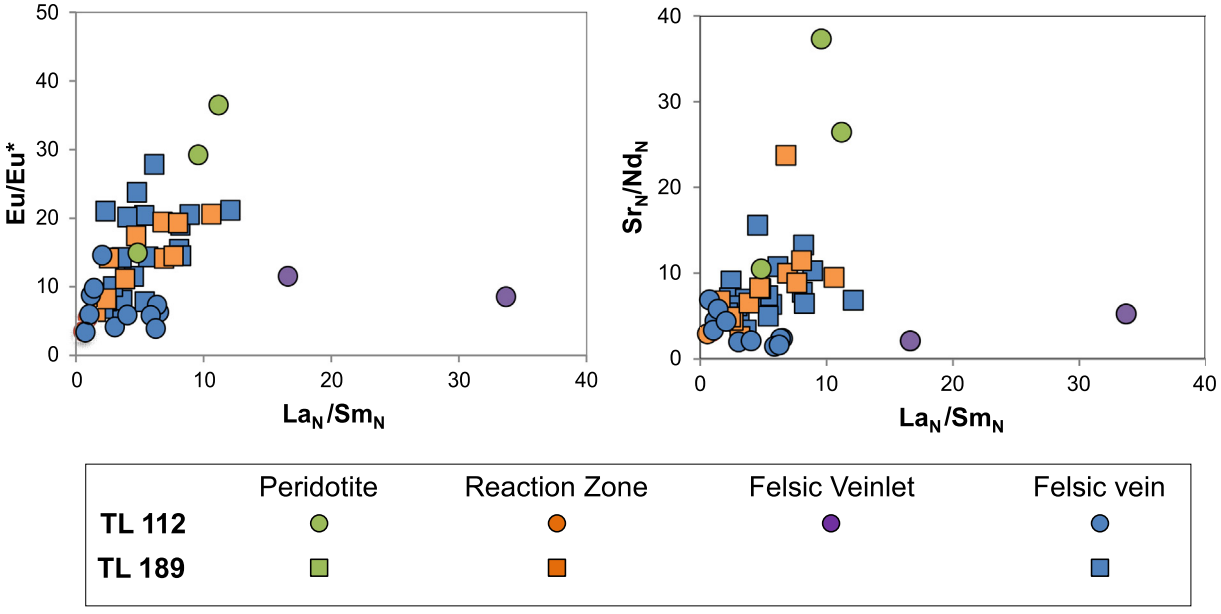

Fig. 7. Chondrite-normalised trace element ratios of plagioclase from the studied composite xenoliths: a) La_N/Sm_N. vs. Eu/Eu*; b) La_N/Sm_N. vs. Sr_N/Nd_N. Normalising values after Sun (1989).

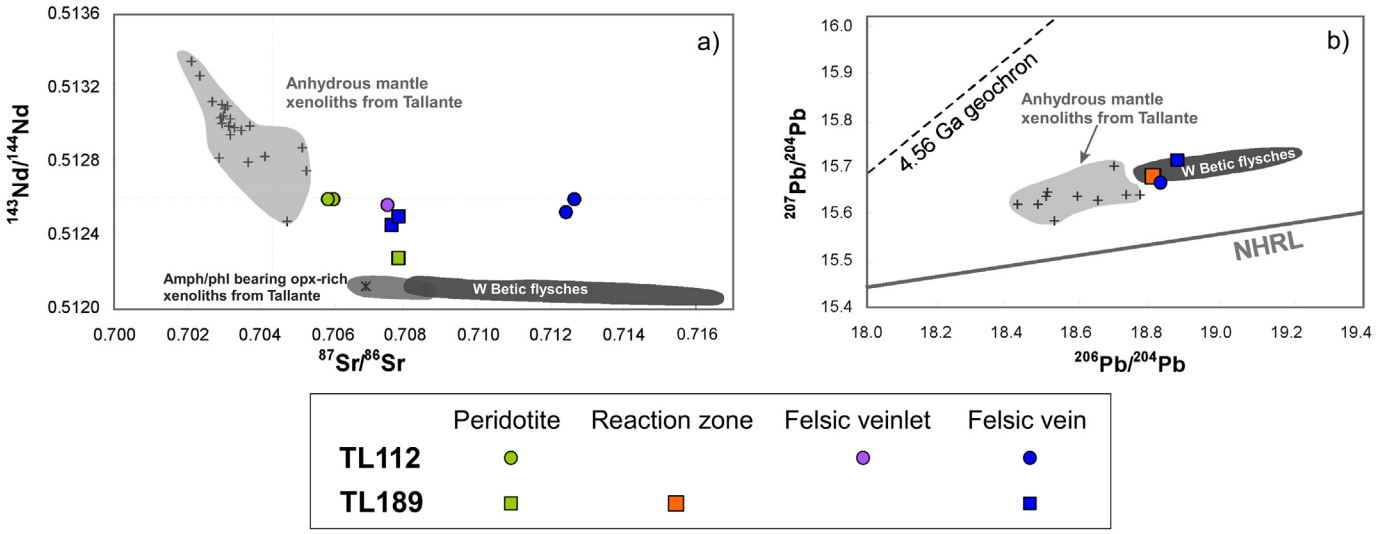

Fig. 8. Isotopic composition of the studied composite mantle xenoliths (data from Table 3) in comparison with published data for other anhydrous (data from Beccaluva et al., 2004, Bianchini et al., 2011, Marchesi et al., 2017 and Dallai et al., 2019). Fields representative of the isotope composition of Western Betic Flysch are drawn from Varas-Reus et al., 2017; a) $^{87}Sr/^{86}Sr$ vs. $^{143}Nd/^{144}Nd$; b) $^{206}Pb/^{204}Pb$ vs. $^{207}Pb/^{204}Pb$: the black line passing through the samples is the North Hemisphere Reference Line (NHRL) calculated from the equation of Hart (1984).

(NHRL: Hart, 1984), which can be used as a proxy for the oceanic mantle array (Fig. 8). This results in $\Delta^{7/4}Pb$ values (i.e., difference between the $^{207}Pb/^{204}Pb$ of the studied samples and the value of the Northern Hemisphere Reference Line at the same $^{206}Pb/^{204}Pb$) as high as 17, hence implying an "old", continental crust origin for the metasomatic agent responsible for the vein formation. The Pb isotope ratios measured in this work are more radiogenic than the compositions obtained on Tallante bulk xenoliths by Marchesi et al. (2017) (Fig. 8).

The same hypothesis can be inferred from the radiogenic Sr and unradiogenic Nd isotope ratios measured in both composite xenolith samples. In fact, the isotope values of the studied xenoliths, even in their peridotite portions, are clearly distinct from those recorded in unveined anhydrous Tallante xenoliths ($^{87}Sr/^{86}Sr$ 0.70213–0.70476, $^{143}Nd/^{144}Nd$ 0.51248–0.51339; Beccaluva et al., 2004; Bianchini et al., 2011), clearly reflecting metasomatic reaction induced by the veining metasomatic agent.

The different distribution of Sr isotopes within the two samples (Fig. 9) and the relative variation of Sr and Nd (Fig. 8), provide interesting clues on the distinct elemental behaviour during the development of metasomatic reactions.

As evident in Fig. 9, in sample TL112 the Sr isotope ratios decrease away from the vein into the reaction zone and the peridotite; the millimetric veinlet has values comparable to those of the reaction zone. In the same sample, however, Nd isotopes do not vary too much between the different zones. On the contrary, in sample TL189 $^{87}Sr/^{86}Sr$ remains rather constant from the vein to the peridotite at values intermediate between those registered in sample TL112 (Fig. 9). In this sample $^{143}Nd/^{144}Nd$ is generally lower than that of TL112, especially in the peridotite portion.

5. Discussion

5.1. Subduction related origin and peculiarity of the composite xenolith of Tallante

Mantle xenoliths from convergent plate settings are rare if compared with those from intra-plate setting (Downes, 2001; Pearson et al., 2003). On the other hand, evidence of subduction related components have often been observed in orogenic peridotite massifs. However, in these cases it is difficult to discern if metasomatism occurred at mantle depths or at crustal levels during complex P-T-t paths that ultimately led to exhumation (Förster et al., 2017; Li et al., 2018).

For these reasons the few findings of xenoliths from convergent settings have attracted significant petrological interest (Bali et al., 2008; Bénard and Ionov, 2013; Conticelli and Peccerillo, 1990; Cvetković et al., 2007; Ducea and Saleby, 1998; Franz et al., 2002; Ishimaru and

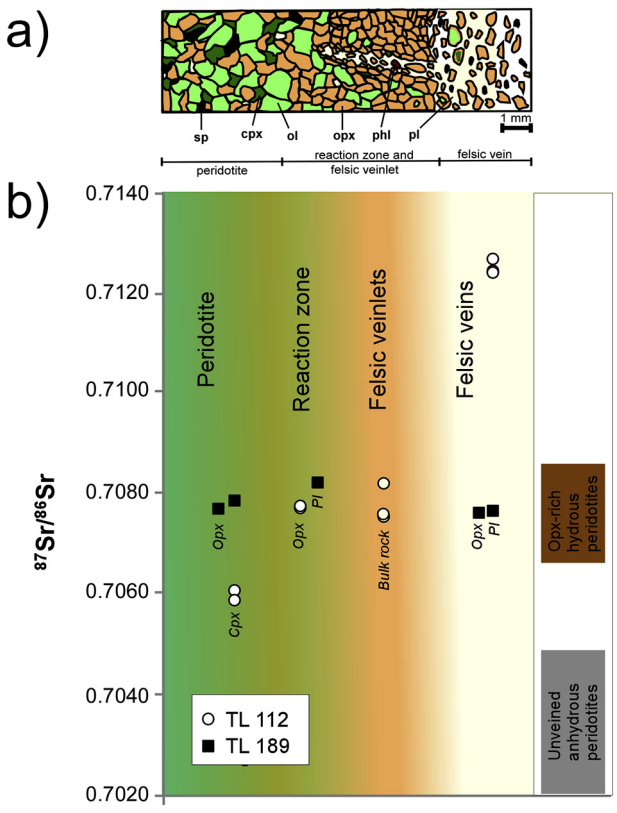

Fig. 9. a) Petrographic sketch of lithological and petrographic variations observed in the composite mantle xenoliths from Tallante; b) Strontium isotope variation of minerals in the studied samples; errors (2 s.e.) are smaller than symbol size. The strontium isotopic range of unveined anhydrous and opx-rich hydrous peridotite mantle xenoliths from Tallante is also reported (data from Beccaluva et al., 2004 and Bianchini et al., 2011).

Arai, 2009; Kepezhinskas et al., 1995; Maury et al., 1992; Takahashi, 1986). Most of these studies suggested that subduction-related metasomatism in convergent setting are induced by silicic melts, which convert olivine in orthopyroxene inducing contemporaneous crystallisation of alkali-repository metasomatic phases such as amphibole or phlogopite. However, the exact nature of the metasomatic agent still remains largely elusive.

In this view, the xenolith suite from Tallante represents a unique case in which peridotite is crosscut by quartz + plagioclase + orthopyroxene-bearing felsic veins up to centimetric in width, embedded in an orthopyroxene-rich metasomatic aureola (e.g., Arai et al., 2003; Beccaluva et al., 2004; Bianchini et al., 2011; Shimizu et al., 2004). The uniqueness of these metasomatic parageneses is also given by the presence of graphite, amphibole, phlogopite plus a plethora of accessory minerals such as apatite, monazite, thorite/huttonite, zircon and rutile that have never been observed in other mantle xenolith suites so far. These mineralogical characteristics can be explained by the interaction between a percolating silica-oversaturated melt and the surrounding peridotite inducing consumption of olivine and clinopyroxene to produce orthopyroxene and plagioclase, according to the following reactions (Kelemen et al., 1998; Prouteau et al., 2001):

$$(Mg,Fe)_2SiO_4 + SiO_2 - \text{rich melt}_1 = (Mg,Fe)_2Si_2O_6 + \text{melt}_2$$

and

$$Ca(Mg,Fe)Si_2O_6 + (Mg,Fe)Al_2O_4 + SiO_2 - \text{rich melt}_1 = (Ca,Na)Al_{2-1}Si_{3-2}O_8 + (Mg,Fe)_2Si_2O_6 + SiO_2 \pm \text{melt}_2$$

The two reactions focus only on the metasomatic transformation of olivine, clinopyroxene, and spinel into orthopyroxene, plagioclase, and quartz, not taking into account the fact that metasomatic melts carry a notable amount of alkalis that may stabilise either amphibole or phlogopite in the metasomatised veins (e.g., Foley, 1992). Notably, the variable amount of alkalis and the X_{CO2} of the metasomatising melts are responsible for the different potassium-enrichment and silica-saturation degree of the magmas in the collisional magmatism of the Central-Western Mediterranean (e.g., Avanzinelli et al., 2009; Conticelli et al., 2009, 2015; Foley, 1992; Mattei et al., 2014, and references therein).

The alkali-rich and silica-rich melts rising up and percolating suprasubduction mantle regions are highly reactive and thus interact extensively with the surrounding mantle minerals, likely changing their trace element composition as the reaction proceeds (Kepezhinskas et al., 1995; Prouteau et al., 2001). The centimetric veins might represent portions of the mantle with the highest melt/wall rock proportion, which instead decreases towards the reaction zone and the surrounding peridotite. The millimetric veinlet can represent apophyses of bigger veins deriving from the interaction of the mantle peridotite with small amounts of an extremely residual melt fraction enriched in the most incompatible trace elements.

In this process the minerals hosted in the vein more closely reflect the geochemical and isotope composition of the percolating melt. The extremely radiogenic $^{87}Sr/^{86}Sr$ and unradiogenic $^{143}Nd/^{144}Nd$ of the minerals within the centimetric felsic veins, as well as their Pb isotope composition (i.e., high $\Delta^{7/4}Pb$ values) provide strong evidence for the origin of the percolating melt being derived from recycled continental crust material into the mantle wedge via subduction.

The new Sr—Nd isotopic data are coherent with those already available in the literature (Beccaluva et al., 2004; Dallai et al., 2019) and with other isotope systematics carried out on Tallante xenoliths (i.e., hafnium and helium isotopes: Bianchini et al., 2011; Martelli et al., 2011) that invariably indicate the involvement of crustal lithologies. Moreover, a recent study from Dallai et al. (2019), recorded extremely high $\delta^{18}O$ in mantle xenoliths from Tallante, confirming the crustal origin of the metasomatic melts, with the highest $\delta^{18}O$ values (10.56 in plagioclase and 9.84 in orthopyroxene) measured in the vein of the same composite xenolith investigated in this study (i.e., TL112). Further evidence for a subduction-derived origin of the percolating melt is provided by the trace elements of the measured mineral phases. All the studied mineral phases are extremely enriched in M- and H-REE with respect to the composition of the same phases in anhydrous xenoliths samples (Fig. 6). In particular, clinopyroxenes have strongly fractionated MREE/HREE patterns that require the interaction with a percolating melt deriving from a garnet-bearing lithology (Warren et al., 2018), that is consistent with the composition (and residual mineralogy) reported for experimental melting of sedimentary lithologies at subduction-like conditions (e.g., Skora et al., 2015).

It is reasonable to postulate that the metasomatised felsic melts are related to partial melting of subducted continental crust lithologies having a lower solidus condition with respect to peridotites. Volcanic activity at Tallante also exhumed garnet-bearing metasedimentary xenoliths, equilibrated at P-T conditions (0.7 GPa, 1100 °C, Bianchini et al., 2015) similar to those of the coexisting mantle xenoliths (850 °C–1050 °C and 0.7–0.9 GPa: Rampone et al., 2010; Bianchini et al., 2011 and references therein). They have silica/alumina-rich bulk compositions, consist mainly of quartz, plagioclase, garnet, spinel, ilmenite ± orthopyroxene ± sillimanite ± graphite, and are characterised by trace elements budget indicating the occurrence of partial melting and melt extraction (Bianchini et al., 2015 and references therein). These metasedimentary xenoliths also contain glassy films of andesitic composition (up to 60 wt% SiO_2), representing quenched melt fractions potentially having plagioclase and orthopyroxene as early liquidus phases, which resemble the mineralogy of felsic veins observed in composite xenoliths.

We therefore suggest that the felsic veins crosscutting peridotite at Tallante are related to anatexis of crustal lithologies. The anatectic processes do not occur at shallow levels, but are likely confined close to the MOHO interface, where crustal and peridotite domains are intimately inter-fingered and juxtaposed during continental collision, forming crust-mantle melanges. The proposed hypothesis fits the evidence observed in metasedimentary xenoliths from other neighbouring volcanic regions in which migmatisation has been observed (Cesare and Gómez-Pugnaire, 2001).

5.2. Extent and mechanism of mantle metasomatism

Constraints on the mechanism of mantle metasomatism and its effect on the mineral phases of the modified mantle can be obtained by comparing the isotopic and elemental composition of the different mineral phases and of the different portion of the studied xenoliths.

The peculiar trace element enrichment and distribution found in the pyroxenes from the peridotite portion of both xenoliths, as well as their isotope composition, clearly indicate that the effect of the metasomatic agent is not limited to the vein and the surrounding reaction zone, but it extends also into the surrounding peridotite. The M-shaped REE patterns of clinopyroxene can be explained by a twofold type of control, namely: i) the composition of the percolating melt, and ii) the trace element re-distribution in the mineral phases stabilised during the melt rock interaction.

The composition of the percolating melt in equilibrium with clinopyroxene is often calculated on the basis of partition coefficients taken from the literature. In our case it is difficult to assess a correct (and complete) set of partition coefficients, considering that the silica-rich melt must have changed its composition continuously due to the interaction with the peridotite matrix. In Fig. 10 we plot the hypothetic composition of melts in equilibrium with clinopyroxene using two different sets of partition coefficients, for a percolating mafic melt (Lee et al., 2007) and for a more evolved one (Fujimaki et al., 1984). Both patterns show extreme MREE enrichment and clearly fractionated M- to HREE that can be interpreted as deriving from partial melting of subducted crustal material in the presence of residual garnet. The

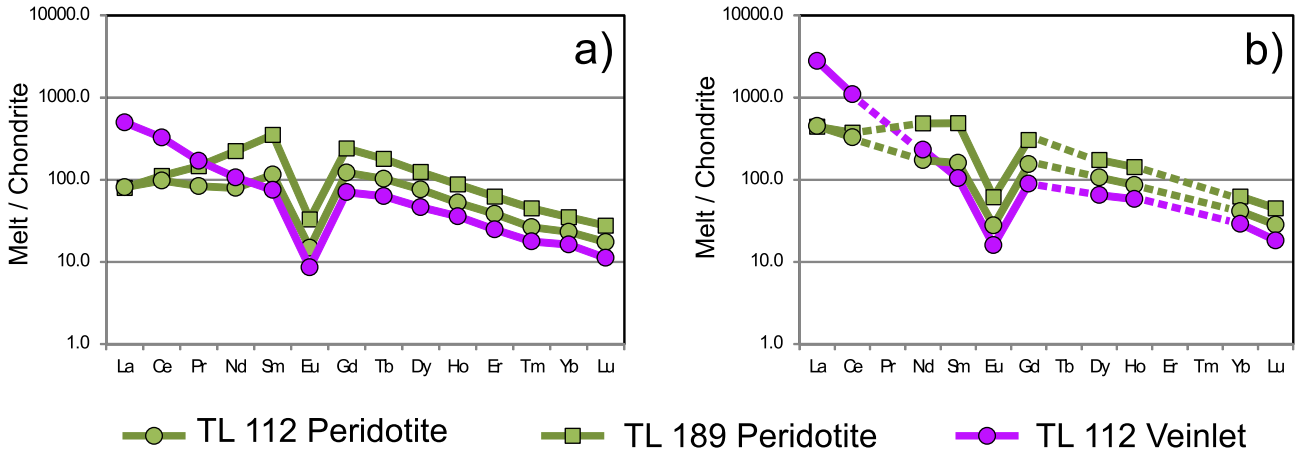

Fig. 10. Chondrite-normalised Rare Earth Element (REE) abundances of melts in equilibrium with clinopyroxene calculated with two sets of clinopyroxene/liquid partition coefficients, namely a) Lee et al. (2007), for basaltic compositions and b) Fujimaki et al. (1984), for dacitic composition. Normalising values after Sun (1989).

other common feature is the presence of a clear Eu negative anomaly that is likely related to the contemporaneous crystallisation of plagioclase, mainly in the vein and, to a lesser extent, in the reaction zone. The distribution of the LREE in the calculated melts is different depending on the set of partition coefficients used. With partition coefficients calculated for dacite (Fujimaki et al., 1984), LREE of the calculated melts are slightly enriched. On the contrary, using the other set of partition coefficients, they appear significantly less enriched than MREE, with La_N/Sm_N ratios generally lower than one. In both cases however, the extent of LREE enrichment is less marked than what would be expected for a crustal melt (e.g., Skora et al., 2015), even after interacting with mantle peridotite. LREE, however, are relatively enriched in the measured plagioclase as evident in Fig. 6. Therefore, the same process responsible for the Eu (and Sr) depletion in pyroxenes can affect, although to a lesser extent, the LREE distribution of the calculated melts. Indeed, the overall distribution of REE in plagioclase mirrors almost perfectly that of clinopyroxene. Clinopyroxene from the felsic veinlet of TL112 shows more enriched LREE, and consequently yields larger LREE/MREE fractionation in the calculated melts in equilibrium. This is consistent with this veinlet representing a residual melt probably more enriched in LREE.

The trace element distribution among the mineral phases stabilising in this metasomatised mantle, and the different proportion of the percolating melt and the surrounding peridotite are also important features to understand the isotope variability between the different zones and, in particular, the different behaviour of Sr and Nd isotopes in sample TL112. In this sample $^{87}Sr/^{86}Sr$ strongly decreases from the vein to the peridotite, clearly indicating a decreasing proportion of "metasomatic" radiogenic Sr away from the vein. On the contrary, Nd isotopes show little variation preserving low $^{143}Nd/^{144}Nd$ also in the peridotite portion. This different behaviour can be explained in the framework of reactive porous flow, where the mobility of Sr and Nd through the peridotite depends on the mineral phases formed during the metasomatic process and their partition coefficients. In this process most of the radiogenic Sr from the crustal felsic melt is locked into plagioclase, mainly in the vein. Therefore, as long as the proportion between percolating melt and surrounding peridotite decreases away from the vein, the isotope ratio decreases coherently (as well as the modal amount of metasomatic plagioclase). Nd instead is not held in the main mineral phases stabilising in the vein (and in the reaction zone) and thus it remains extremely enriched in the percolating melt. The clinopyroxene in the peridotite reacts with this Nd rich crustal melt, resulting in its MREE enrichment and also attaining the crustal isotopic signature of the percolating melt.

5.3. Role of diffusion-driven isotope equilibration

The distribution of isotope ratios in the studied xenoliths could also be affected by diffusion driven isotope re-equilibration after the occurrence of metasomatism.

Sample TL112 clearly preserves a significant variation in Sr isotope ratios among the different zones of the composite xenoliths. The observed variations cannot be due to ^{87}Sr decay from ^{87}Rb, since no relationship is observed between Rb/Sr ratios and Sr isotope ratios (not shown). In fact, the highest $^{87}Sr/^{86}Sr$ were measured in plagioclase separates that have the lowest Rb/Sr ratios. Therefore, the observed variation must be related to the original heterogeneity of the metasomatised mantle, which must have not restored Sr isotopic equilibrium.

A similar variation in sample TL112 was observed for oxygen isotopes by Dallai et al. (2019), with $\delta^{18}O$ decreasing significantly from the vein to the surrounding peridotite portion. The same study calculated that after about 5 million years oxygen isotopes should have completely re-equilibrated, hence implying that the metasomatic process that produced the isotopic variation observed in TL 112 must have occurred shortly before the eruption of the composite xenoliths.

This de facto eliminates also the possibility that the little variation observed in Nd isotope ratios could be related to diffusion processes. Indeed, a study from Van Orman et al. (2001) indicates that at relatively low temperature and pressure (1150 °C, 1GPa), similar to the ones estimated for the Tallante xenoliths (850 °C–1050 °C and 0.7–0.9 GPa: Rampone et al., 2010; Bianchini et al., 2011 and references therein) the time required for Nd isotopic equilibration is extremely long, up 1000 Ma. Such a long time is clearly inconsistent with the variability observed in Sr and oxygen isotopes in the same samples.

Data for Sr diffusion in clinopyroxene (Sneeringer et al., 1984) and orthopyroxene (Cherniak and Liang, 2007) indicate that Sr isotope composition re-equilibrate faster than Nd. According to these studies isotopic equilibration at the mineral (mm) scale should occur in a few million years (Cherniak and Liang, 2007; Sneeringer et al., 1984), or even faster when considering possible diffusion along grain boundaries.

Therefore, the observed variability in Sr isotope ratios between the different zones of the studied composite xenolith TL112 constrains the veining process to have occurred shortly before the xenolith eruption, in agreement with oxygen isotope data.

Sample TL189 shows trace element patterns similar to sample TL112 and it also shows radiogenic Sr and unradiogenic Nd isotope ratios, confirming a similar style of metasomatism related to the interaction with felsic melt deriving from subducted crustal material. Differently

from TL112, however, in TL189 the Sr isotope ratios are rather constant from the vein to the surrounding peridotite. According to the discussion above, this sample could represent a portion of the lithospheric mantle where the heterogeneities in $^{87}Sr/^{86}Sr$ induced by metasomatism had sufficient time (few million years) to re-equilibrate at the xenolith scale through diffusion. If this is true, it would imply that the lithospheric mantle beneath the Betic area had been affected by different events of crustal-derived felsic metasomatism over a time span of a few millions years. In this scenario, the studied xenoliths represent portions of the lithospheric mantle affected by similar processes at different times, yet still in the geodynamic framework of the Tertiary closure of the western Tethys Ocean and subsequent continental collisions that involved Africa and Eurasia.

6. Conclusive remarks

6.1. Geodynamic inferences

The new Sr-Nd-Pb isotopic and trace element data are coherent with those already available in the literature (Beccaluva et al., 2004) and with other isotope systematics carried out on Tallante xenoliths (Bianchini et al., 2011; Dallai et al., 2019; Martelli et al., 2011). In fact, hafnium isotopic analyses in Tallante xenoliths revealed the most unradiogenic isotopic composition ever found in mantle rocks. Similarly, helium and oxygen isotopic analyses invariably recorded low $^{3}He/^{4}He$ and high $\delta^{18}O$ compositions typical of continental crust lithologies. These geochemical features imply a significant recycling of continental crust lithologies via subduction, which is a scenario recently proposed by geochemical studies on the Betic metamorphic basement (Varas-Reus et al., 2017). In their study, Varas-Reus et al. (2017) also report isotopic data on several crustal lithologies and sediments outcropping in the western Betics, some of which (i.e., the Flysch Units) have isotopic composition compatible with those found in the studied xenoliths (Fig. 10). The same crustal units were indicated by the authors as the most likely subducted end-members that released fluids or partial melts into the lithospheric mantle inducing the isotopic signature of the subduction-related magmas erupted in the area.

Considering the extreme geochemical and isotopic heterogeneity recorded in the various types of xenoliths erupted at Tallante (Fig. 8), as well as the different timescales discussed in the previous section, we suggest a scenario where the lithospheric mantle underlying the Betic region has been characterised by long-lasting processes where different crustal melts affected the mantle at different times, until the xenolith exhumation.

The proposed scenario (Fig. 11) occurred during the late-stage of plate convergence, when subduction is followed by continental collision with inter-layering of mantle and continental slivers including low solidus crustal lithologies. Coherently, crust-mantle melanges are observed in the neighbouring massifs of Ronda and Beni Bousera, where the exhumed fossil Crust Mantle Boundary (CMB) is characterised by mylonites and melanges (e.g., Platt et al., 2013; Tubía et al., 2004). These mylonitic domains could reflect deep shear zones that favour inter-fingering/juxtaposition of distinct crustal and mantle lithologies. The hypothesis is supported by seismic profiles of the Betic area that have highlighted the occurrence of heterogeneous seismic velocities beneath the CMB (at the depth of 22–23 km: De Larouzière et al., 1988). Similar cases of interlayered crust–mantle associations occur throughout the peri-Mediterranean region, such as in the fossil deep crust–mantle sections of the Ivrea-Verbano (Quick et al., 1995), the Ulten Zone (Braga and Massonne, 2012) and central Calabria (Rizzo et al., 2001).

The hypothesis is consistent with field evidence and analogue and numerical experiments indicating that indentation of mantle and crustal rocks may occur in supra-subduction settings (e.g., Brueckner, 1998; Burov et al., 2014; Gerya and Yuen, 2003), during continental collision and subsequent delamination of the thickened lithosphere (Tubía et al., 2004) or in post-collisional settings (Harris et al., 2012).

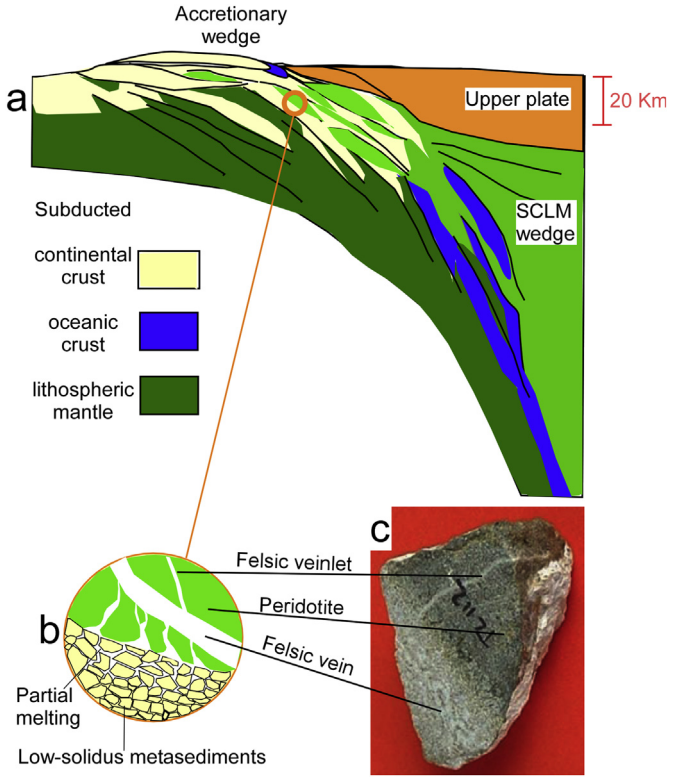

Fig. 11. Cartoon showing a sketch of crustal recycling related to crust-mantle interlayering during continental collision (a). Partial melting of the crustal domains generates felsic melts that percolate through the peridotite domains. These silica-rich melts react with the surrounding peridotite (b) and freeze to form the felsic metasomatic veins and the residual veinlets, as found in the studied composite mantle xenolith of Tallante (c). Modified after Dallai et al. (2019).

In the presence of such crust mantle melanges, silica-rich melts could form from the low solidus lithologies contained in crustal domains, and in response to upraising of the isotherms related to the crustal and lithospheric thinning and associated mantle uplift produced during back-arc extension (e.g., Platt et al., 2013. Such a process could also be aided by local decompression related to episodes of back-arc basin inversion such as those suggested by Varas-Reus et al. (2017). These crustal melts segregate from their sources and interact with the surrounding mantle domains, producing the metasomatic reactions observed in the studied xenoliths.

The same process could explain the felsic dykes of Miocene age crosscutting the peridotite bodies of Ronda and Beni Bousera (Rossetti et al., 2010 and references therein), which may represent large-scale analogues of the centimetric veins observed in the studied mantle xenoliths from Tallante.

6.2. Inferences for magma-genesis in post-collisional settings

The studied mantle xenoliths provide key evidence to explain the genesis of post-orogenic calc-alkaline to ultrapotassic magmatism of the Betic region.

Similarly to other volcanic associations of the Western Mediterranean (e.g., Western Alps, Corsica, and Tuscany), the Betic volcanism was characterised by low- to high potassium volcanic products in close spatial-temporal association (e.g. Cabo de Gata volcanic rocks and Murcia lamproites: Duggen et al., 2005; Prelević et al., 2008; Conticelli et al., 2009, Mattei et al., 2014).

Of particular note is that many of the Western Mediterranean volcanic rocks associated with destructive plate margins record a time-related transition from potassic to calc-alkaline volcanism (e.g., Avanzinelli et al., 2009; Conticelli et al., 2009, 2015; Mattei et al., 2014). Such a transition reflects re-equilibration of the isotherms in a post-collisional environment and progressive evolution of the magma sources within a sub-continental lithospheric mantle variously crosscut by veins as shown by the mantle xenoliths investigated in this study.

Partial melting of such veined mantle first affects the metasomatic veins (that are characterised by low-solidus temperatures) and continues progressively involving also the surrounding ambient peridotite as the temperature increases. The delineated hypothesis thus explains the progressive dilution of the vein metasomatic components, and the related vanishing of subduction-related geochemical and isotopic signature in the erupted magmas (e.g., Avanzinelli et al., 2009; Conticelli et al., 2009; Foley, 1992; Mattei et al., 2014).

In this scenario, our study presents the first direct evidence for the presence of a veined lithospheric mantle, perfectly consistent with the source suggested to explain the geochemical and isotopic variation recorded in the calc-alkaline to ultrapotassic magmas of the Betic area. Our data show that the geochemical and isotopic crustal signature is mostly concentrated within the veins, but it permeates also the peridotite portion of the modified lithospheric mantle. Therefore, melts deriving from different proportion of vein and surrounding peridotite will inherit variable levels of trace element and isotopic enrichment. Yet, a general crustal flavour will be preserved also in higher degree melts where the vein is almost exhausted or its contribution is highly diluted from the surrounding peridotite.

The presented data also argues against consolidated petrological tenets that strictly relate the isotopic composition of magmas to those of the related magma sources. In fact, disequilibrium melting of veined mantle sources characterised by isotopic heterogeneities is strictly dependent on the mantle phases that prevalently contribute to the melting.

The effectiveness of the proposed petrological hypothesis is not restricted to the orogenic volcanism of the Betic area, but it fits and conforms magma genesis in several volcanic districts of the whole Alpine-Himalayan belt where complex orogenic association of magma types are usually recorded.

Declaration of Competing Interest

The authors declare that they have no known competing financial interests or personal relationships that could have appeared to influence the work reported in this paper.

Acknowledgements

The authors thank Stefano Poli, Andrea Risplendente and Anna Maria Fioretti for allowing access at the EMPA facilities of Milan and Padua, Maurizio Ulivi for technical support during SEM and Sr-Nd-Pb isotope analyses at the Dipartimento di Scienze della Terra of the University of Florence, and Leone Melluso and Roberto De Gennaro for SEM analyses at the Geological Sciences Department of the University of Naples Federico II. Dr. Derek Keir is also thanked for the proofreading of the manuscript. Thorough and thoughtful reviews by Carlos Villaseca and Paolo Sossi greatly improved the manuscript. Financial support was provided by Italian MIUR through the PRIN 2010-11 and 2015 funding, grants # 2010TT22SC and # 20158A9CBM issued to SC and grant 2015EC9PJ5 issued to RA.

Appendix A. Supplementary data

Supplementary data to this article can be found online at https://doi.org/10.1016/j.lithos.2019.105316.

References

Ammannati, E., Jacob, D.E., Avanzinelli, R., Foley, S.F., Conticelli, S., 2016. Low Ni olivine in silica-undersaturated ultrapotassic igneous rocks as evidence for carbonate metasomatism in the mantle. Earth Planet. Sci. Lett. 444, 64–74.

Arai, S., Shimizu, Y., Gervilla, F., 2003. Quartz diorite veins in a peridotite xenolith from Tallante, Spain: implications for reactions and survival of slab-derived SiO2-oversaturated melts in the upper mantle. Proce. Japan Acad. Series B 79, 145–150.

Avanzinelli, R., Boari, E., Conticelli, S., Francalanci, L., Guarnieri, L., Perini, G., Petrone, C.M., Tommasini, S., Ulivi, M., 2005. High precision Sr, Nd, and Pb isotopic analyses using the new generation thermal Ionisation Mass Spectrometer ThermoFinnigan Triton-Ti®. Periodico di Mineralogia 74, 147–166.

Avanzinelli, R., Lustrino, M., Mattei, M., Melluso, L., Conticelli, S., 2009. Potassic and ultrapotassic magmatism in the circum-Tyrrhenian region: significance of carbonated pelitic vs. pelitic sediment recycling at destructive plate margins. Lithos 113 (1–2), 213–227.

Bali, E., Zajacz, Z., Kovács, I., Szabó, C., Halter, W., Vaselli, O., Török, K., Bodnar, R.J., 2008. A Quartz-bearing Orthopyroxene-rich Websterite Xenolith from the Pannonian Basin, Western Hungary: evidence for Release of Quartz-saturated Melts from a Subducted Slab. J. Petrol. 49, 421–439.

Beccaluva, L., Bianchini, G., Bonadiman, C., Siena, F., Vaccaro, C., 2004. Coexisting anorogenic and subduction-related metasomatism in mantle xenoliths from the Betic Cordillera (southern Spain). Lithos 75, 67–87.

Bénard, A., Ionov, D.A., 2013. Melt– and fluid–Rock interaction in supra-subduction lithospheric mantle: evidence from andesite-hosted veined peridotite xenoliths. J. Petrol. 54, 2339–2378.

Bianchini, G., Natali, C., 2017. Carbon elemental and isotopic composition in mantle xenoliths from Spain: Insights on sources and petrogenetic processes. Lithos 272-273, 84–91.

Bianchini, G., Beccaluva, L., Bonadiman, C., Nowell, G., Pearson, G., Siena, F., Wilson, M., 2007. Evidence of diverse depletion and metasomatic events in harzburgite–lherzolite mantle xenoliths from the Iberian plate (Olot, NE Spain): Implications for lithosphere accretionary processes. Lithos 94, 25–45.

Bianchini, G., Beccaluva, L., Bonadiman, C., Nowell, G.M., Pearson, D.G., Siena, F., Wilson, M., 2010. Mantle metasomatism by melts of HIMU piclogite components: new insights from Fe-lherzolite xenoliths (Calatrava Volcanic District, Central Spain). Geol. Soc. Lond. Spec. Publ. 337, 107–124.

Bianchini, G., Beccaluva, L., Nowell, G.M., Pearson, D.G., Siena, F., 2011. Mantle xenoliths from Tallante (Betic Cordillera): insights into the multi-stage evolution of the south Iberian lithosphere. Lithos 124, 308–318.

Bianchini, G., Bryce, J.G., Blichert-Toft, J., Beccaluva, L., Natali, C., 2014. Mantle dynamics and secular variations beneath the East African Rift: Insights from peridotite xenoliths (mega, Ethiopia). Chem. Geol. 386, 49–58.

Bianchini, G., Braga, R., Langone, A., Natali, C., Tiepolo, M., 2015. Metasedimentary and igneous xenoliths from Tallante (Betic Cordillera, Spain): inferences on crust–mantle interactions and clues for post-collisional volcanism magma sources. Lithos 220-223, 191–199.

Bonadiman, C., Beccaluva, L., Coltorti, M., Siena, F., 2005. Kimberlite-like Metasomatism and 'Garnet Signature' in Spinel-peridotite Xenoliths from Sal, Cape Verde Archipelago: Relics of a Subcontinental Mantle Domain within the Atlantic Oceanic Lithosphere? J. Petrol. 46, 2465–2493.

Bonadiman, C., Coltorti, M., Beccaluva, L., Griffin, W.L., O'Reilley, S., Siena, F., 2011. Metasomatism versus host magma infiltration: a case study of Sal mantle xenoliths, Cape Verde Archipelago. Geol. Soc. Am. Spec. Pap. 478, 283–305.

Braga, R., Massonne, H.-J., 2012. H2O content of deep-seated orogenic continental crust: the Ulten Zone, Italian Alps. Int. Geol. Rev. 54, 633–641.

Brueckner, H.K., 1998. Sinking intrusion model for the emplacement of garnet-bearing peridotites into continent collision orogens. Geology 26 (7), 631–634.

Burov, E., Francois, T., Yamato, P., Wolf, S., 2014. Mechanisms of continental subduction and exhumation of HP and UHP rocks. Gondwana Res. 25, 464–493.

Cebriá, J.M., López-Ruiz, J., Carmona, J., Doblas, M., 2009. Quantitative petrogenetic constraints on the Pliocene alkali basaltic volcanism of the SE Spain Volcanic Province. J. Volcanol. Geotherm. Res. 185, 172–180.

Cesare, B., Gómez-Pugnaire, M.T., 2001. Crustal melting in the alborán domain: constraints from xenoliths of the Neogene Volcanic Province. Phys. Chem. Earth Part A: Solid Earth. Geodesy 26, 255–260.

Cherniak, D.J., Liang, Y., 2007. Rare Earth element diffusion in natural enstatite. Geochim. Cosmochim. Acta 71, 1324–1340. https://doi.org/10.1016/j.gca.2006.12.001.

Conticelli, S., Peccerillo, A., 1990. Petrological significance of high-pressure ultramafic xenoliths from ultrapotassic rocks of Central Italy. Lithos 24 (4), 305–322.

Conticelli, S., Guarnieri, L., Farinelli, A., Mattei, M., Avanzinelli, R., Bianchini, G., Boari, E., Tommasini, S., Tiepolo, M., Prelević, D., Venturelli, G., 2009. Trace elements and Sr–Nd–Pb isotopes of K-rich, shoshonitic, and calc-alkaline magmatism of the Western Mediterranean Region: genesis of ultrapotassic to calc-alkaline magmatic associations in a post-collisional geodynamic setting. Lithos 107, 68–92.

Conticelli, S., Avanzinelli, R., Ammannati, E., Casalini, M., 2015. The role of carbon from recycled sediments in the origin of ultrapotassic igneous rocks in the Central Mediterranean. Lithos 232, 174–196.

Cvetković, V., Lazarov, M., Downes, H., Prelević, D., 2007. Modification of the subcontinental mantle beneath East Serbia: evidence from orthopyroxene-rich xenoliths. Lithos 94 (1), 90–110.

Dallai, L., Bianchini, G., Avanzinelli, R., Natali, C., Conticelli, S., 2019. Heavy oxygen recycled into the lithospheric mantle. Sci. Rep. – Nat. 9 (1), 8793.

De Larouzière, F.D., Bolze, J., Bordet, P., Hernandez, J., Montenat, C., Ott D'estevou, P., 1988. The Betic segment of the lithospheric Trans-Alboran shear zone during the late Miocene. Tectonophysics 152, 41–52.

Di Salvo, S., Braschi, E., Casalini, M., Marchionni, S., Adani, T., Ulivi, M., Orlando, A., Tommasini, S., Avanzinelli, R., Mazza, P.P.A., Conticelli, S., Francalanci, L., 2018. High-precision In Situ 87Sr/86Sr analyses through microsampling on solid samples: applications to earth and life sciences. J. Anal. Methods. Chem. 20 ID 1292954.

Doblas, M., López-Ruiz, J., Cebriá, J.M., 2007. Cenozoic evolution of the Alboran domain: a review of the tectono magmatic models. In: Beccaluva, L., Bianchini, G., Wilson, M. (Eds.), Volcanism in the Mediterranean Area. Geological Society of America, pp. 303–320.

Downes, H., 2001. Formation and modification of the shallow sub-continental lithospheric mantle: a review of geochemical evidence from ultramafic xenolith suites and tectonically emplaced ultramafic massifs of Western and Central Europe. J. Petrol. 42, 233–250.

Ducea, M., Saleby, J., 1998. Crustal recycling beneath continental arcs: silica rich glass inclusions in ultramafic xenoliths from the Sierra Nevada (California). Earth Planet. Sci. Lett. 156, 101–116.

Duggen, S., Hoernle, K., van den Bogaard, P., Garbe-Schönberg, D., 2005. Post-collisional transition from subduction- to intraplate type magmatism in the westernmost Mediterranean: evidence for continental-edge delamination of subcontinental lithosphere. J. Petrol. 46, 1155–1201.

Faccenna, C., Piromallo, C., Crespo-Blanc, A., Jolivet, L., Rossetti, F., 2004. Lateral slab deformation and the origin of the western Mediterranean arcs. Tectonics 23 TC1012.

Foley, S., 1992. Vein-plus-wall-rock melting mechanisms in the lithosphere and the origin of potassic alkaline magmas. Lithos 28 (3–6), 435–453.

Foley, S.F., Jacob, D.E., O'Neill, H.S.C., 2011. Trace element variations in olivine phenocrysts from Ugandan potassic rocks as clues to the chemical characteristics of parental magmas. Contrib. Mineral. Petrol. 162 (1), 1–20.

Förster, B., Braga, R., Aulbach, S., Lo Po', D., Bargossi, G.M., Mair, V., 2017. A petrographic study of carbonate phases in the Ulten Zone ultramafic rocks: insights into carbonation in the mantle wedge and exhumation-related decarbonation. Ofioliti 42, 105–127.

Franz, L., Becker, K.-P., Kramer, W., Herzig, P., 2002. Metasomatic mantle xenoliths from the Bismark Microplate (Papua New Guinea)—thermal evolution, geochemistry and extent of slab induced metasomatism. J. Petrol. 43, 315–343.

Fujimaki, H., Tatsumoto, M., Aoki, K., 1984. Partition coefficients of Hf, Zr, and REE between phenocrysts and groundmasses. J. Geophys. Res. 89, 662–672.

Gerya, T.V., Yuen, D.A., 2003. Rayleigh–Taylor instabilities from hydration and melting propel 'cold plumes' at subduction zones. Earth Planet. Sci. Lett. 212, 47–62.

Harris, L.B., Godin, L., Yakymchuk, C., 2012. Regional shortening followed by channel flow induced collapse: a new mechanism for "dome and keel" geometries in Neoarchaean granite-greenstone terrains. Precambrian Res. 212–13, 139–154.

Hart, S.R., 1984. A large-scale isotope anomaly in the Southern Hemisphere mantle. Nature 309, 753–757.

Holland, T., Blundy, J., 1994. Non-ideal interactions in calcic amphiboles and their bearing on amphibole-plagioclase thermometry. Contrib. Mineral. Petrol. 116, 433–447.

Ionov, D.A., Bénard, A., Plechov, P.Y., Shcherbakov, V.D., 2013. Along-arc variations in lithospheric mantle compositions in Kamchatka, Russia: first trace element data on mantle xenoliths from the Klyuchevskoy Group volcanoes. J. Volcanol. Geotherm. Res. 263, 122–131.

Ishimaru, S., Arai, S., 2009. Highly silicic glasses in peridotite xenoliths from Avacha volcano, Kamchatka arc, implications for melting and metasomatism within the sub-arc mantle. Lithos 107, 93–106.

Kelemen, P.B., Hart, S.R., Bernstein, S., 1998. Silica enrichment in the continental upper mantle via melt/rock reaction. Earth Planet. Sci. Lett. 164, 387–406.

Kepezhinskas, P.K., Defant, M.J., Drummond, M.S., 1995. Na metasomatism in the island arc mantle by slab melt– peridotite interaction: evidence from mantle xenoliths in the North Kamchatka arc. J. Petrol. 36, 1505–1527.

Lee, C.-T.A., Harbert, A., Leeman, W.P., 2007. Extension of lattice strain theory to mineral/mineral rare-earth element partitioning: an approach for assessing disequilibrium and developing internally consistent partition coefficients between olivine, orthopyroxene, clinopyroxene and basaltic melt. Geochim. Cosmochim. Acta 71, 481–496.

Li, H.-Y., Chen, R.-X., Zheng, Y.-F., Hu, Z., Xu, L., 2018. Crustal metasomatism at the Slab-Mantle interface in a continental subduction channel: geochemical evidence from orogenic peridotite in the Sulu Orogen. J. Geophys. Res. Solid Earth 123, 2174–2198.

Marchesi, C., Konc, Z., Garrido, C.J., Boschc, D., Hidas, K., Varas-Reus, M.I., Acosta-Vigil, A., 2017. Multi-stage evolution of the lithospheric mantle beneath the westernmost Mediterranean: Geochemical constraints from peridotite xenoliths in the eastern Betic Cordillera (SE Spain). Lithos 276, 75–89.

Martelli, M., Bianchini, G., Beccaluva, L., Rizzo, A., 2011. Helium and argon isotopic compositions of mantle xenoliths from Tallante and Calatrava, Spain. J. Volcanol. Geotherm. Res. 200, 18–26.

Mattei, M., Riggs, N.R., Giordano, G., Guarnieri, L., Cifelli, F., Soriano, C.C., Jicha, B., Jasim, A., Marchionni, S., Franciosi, L., Tommasini, S., Porreca, M., Conticelli, S., 2014. Geochronology, geochemistry and geodynamics of the Cabo de Gata volcanic zone, Southeastern Spain. Ital. J. Geosci. 133, 341–361.

Maury, R.C., Defant, M.J., Joron, J.-L., 1992. Metasomatism of the sub-arc mantle inferred from trace elements in Philippine xenoliths. Nature 360, 661–663.

Morimoto, N., 1989. Nomenclature of pyroxenes. Can. Mineral. 27, 143–156.

Neogi, S., Dasgupta, S., Fukuoka, M., 1998. High P–T polymetamorphism, dehydration melting, and generation of migmatites and granites in the higher Himalayan crystalline complex, Sikkim, India. J. Petrol. 39, 61–69.

Neukampf, J., Ellis, B.S., Magna, T., Laurent, O., Bachmann, O., 2019. Partitioning and isotopic fractionation of lithium in mineral phases of hot, dry rhyolites: the case of the Mesa Falls Tuff, Yellowstone. Chem. Geol. 506, 175–186.

Pearson, D.G., Canil, D., Shirey, S.B., 2003. Mantle samples included in volcanic rocks: xenoliths and diamonds. In: Carlson, R.W. (Ed.), The Mantle and Core: Treatise on Geochemistry. 2, pp. 171–275.

Pérez-Soba, C., Villaseca, C., Orejana, D., Jeffries, T., 2014. Uranium-rich accessory minerals in the peraluminous and perphosphorous Belvís de Monroy pluton (Iberian Variscan belt). Contrib. Mineral. Petrol. 167, 1008.

Platt, J.P., Behr, W.M., Johanesen, K., Williams, J.R., 2013. The Betic-Rif Arc and its orogenic hinterland: a review. Annu. Rev. Earth Planet. Sci. Lett. 41, 14.1–14.45.

Prelević, D., Foley, S.F., Romer, R., Conticelli, S., 2008. Mediterranean tertiary lamproites derived from multiple source components in postcollisional geodynamics. Geochim. Cosmochim. Acta 72 (8), 2125–2156.

Prouteau, G., Scaillet, B., Pichavant, M., Maury, R., 2001. Evidence for mantle metasomatism by hydrous silicic melts derived from subducted oceanic crust. Nature 410, 197–200.

Puga, E., Fanning, M., Díaz de Federico, A., Nieto, J.M., Beccaluva, L., Bianchini, G., Díaz Puga, M.A., 2011. Petrology, geochemistry and U-Pb geochronology of the Betic Ophiolites: inferences for Pangaea break-up and birth of the westernmost Tethys Ocean. Lithos 124, 255–272.

Quick, J.E., Sinigoi, S., Mayer, A., 1995. Emplacement of mantle peridotite in the lower continental crust, Ivrea-Verbano zone, Northwest Italy. Geology 23, 739–742.

Rampone, E., Vissers, R.L.M., Poggio, M., Scambelluri, M., Zanetti, A., 2010. Melt migration and intrusion during exhumation of the Alboran lithosphere: the Tallante mantle xenolith record (Betic Cordillera, SE Spain). J. Petrol. 51, 295–325.

Rampone, E., Borghini, G., Godard, M., Ildefonse, B., Crispini, L., Fumagalli, P., 2016. Melt/rock reaction at oceanic peridotite/gabbro transition as revealed by trace element chemistry of olivine. Geochim. Cosmochim. Acta 190 (2016), 309–331.

Rizzo, G., Piluso, E., Morten, L., 2001. Phlogopite from the Serre ultramafic rocks, Central Calabria, Southern Italy. Eur. J. Mineral. 13, 1139–1151.

Rossetti, F., Theye, T., Lucci, F., Bouybaouène, M.L., Dini, A., Gerdes, A., Phillips, D., Cozzupoli, D., 2010. Timing and Modes of Granite Magmatism in the Core of the Alboran Domain (Rif Chain, Northern Morocco): Implications for the Alpine Evolution of the Western Mediterranean: Tectonics 29, TC2017.

Scott, J.M., Liu, J., Pearson, D.G., Waight, T.E., 2016. Mantle depletion and metasomatism recorded in orthopyroxene in highly depleted peridotites. Chem. Geol. 441, 280–291.

Shimizu, Y., Arai, S., Morishita, T., Yurimoto, H., Gervilla, F., 2004. Petrochemical characteristics of felsic veins in mantle xenoliths from Tallante (SE Spain): an insight into activity of silicic melt within the mantle wedge. Trans. R. Soc. Edinb. Earth Sci. 95, 265–276.

Shimizu, Y., Arai, S., Morishita, T., Ishida, Y., 2005. Geochemical signature of the quartz diorite vein in mantle peridotite xenolith from Tallante, SE Spain: laser-ablation ICP-MS analysis. Ofioliti 30 (2), 263–264.

Shimizu, Y., Arai, S., Morishita, T., Ishida, Y., 2008. Origin and significance of spinel–pyroxene symplectite in lherzolite xenoliths from Tallante, SE Spain. Mineral. Petrol. 94, 27–43.

Skora, S., Blundy, J.D., Brooker, R.A., Green, E.C.R., de Hoog, J.C.M., Connolly, J.A.D., 2015. Hydrous phase relations and trace element partitioning behaviour in Calcareous sediments at subduction-zone conditions. J. Petrol. 56, 953–980.

Sneeringer, M., Hart, S.R., Shimizu, N., 1984. Strontium and samarium diffusion in diopside. Geochim. Cosmochim. Acta 48, 1589–1608.

Sun, S.-S., McDonough, W.F., 1989. Chemical and isotopic systematics of oceanic basalts: implications for mantle composition and processes. In: Saunders, A.D., Norry, M.J. (Eds.), Magmatism in the Ocean Basins. 42. Geological Society of London, Special Publication, pp. 313–345.

Takahashi, E., 1986. Genesis of calc-alkaline andesite magma in a hydrous mantle – crust boundary: petrology of lherzolite xenoliths from the Ichinomegata Crater, Oga Peninsula, Northeast Japan, Part II. J. Volcanol. Geotherm. Res. 29, 355–395.

Tiepolo, M., Bottazzi, P., Palenzona, M., Vannucci, R., 2003. A laser probe coupled with ICP–double-focusing sector-field mass spectrometer for in situ analysis of geological samples and U–Pb dating of zircon. Can. Mineral. 41 (2), 259–272.

Tubía, J.M., Cuevas, J., Esteban, J.J., 2004. Tectonic evidence in the Ronda peridotites, Spain, for mantle diapirism related to delamination. Geology 32, 941–944.

Van Orman, J.A., Grove, T.L., Shimizu, N., 2001. Rare earth element diffusion in diopside: influence of temperature, pressure, and ionic radius, and an elastic model for diffusion in silicates. Contrib. Mineral. Petrol. 141, 687–703.

Varas-Reus, M.I., Garrido, C.J., Marchesi, C., Bosch, D., Acosta-Vigil, A., Hidas, K., Barich, A., Booth-Rea, G., 2017. Sr-Nd-Pb isotopic systematics of crustal rocks from the western Betics (S. Spain): Implications for crustal recycling in the lithospheric mantle beneath the westernmost Mediterranean. Lithos 276, 45–61.

Warren, C.J., Greenwood, L.V., Argles, T.W., Robert, N.M.W., Parrish, R.R., Harris, N.B.W., 2018. Garnet–Monazite Rare Earth Element Relationships in Sub-Solidus Metapelites: A Case Study from Bhutan. Metamorphic Geology: Microscale to Mountain Belts. Geological Society, London, Special Publications, p. 478.

Witt-Eickschen, G., O'Neill, H.S.C., 2005. The effect of temperature on the equilibrium distribution of trace elements between clinopyroxene, orthopyroxene, olivine and spinel in upper mantle peridotite. Chem. Geol. 221 (1), 65–101.